



# Observed Modulation of the Tropical Radiation Budget by Deep Convective Organization and Lower-Tropospheric Stability

S Bony, A Semie, R J Kramer, B Soden, A M Tompkins, K A Emanuel

## ► To cite this version:

S Bony, A Semie, R J Kramer, B Soden, A M Tompkins, et al.. Observed Modulation of the Tropical Radiation Budget by Deep Convective Organization and Lower-Tropospheric Stability. AGU Advances, 2020, 10.1029/2019AV000155 . hal-03022478

**HAL Id: hal-03022478**

**<https://hal.sorbonne-universite.fr/hal-03022478>**

Submitted on 24 Nov 2020

**HAL** is a multi-disciplinary open access archive for the deposit and dissemination of scientific research documents, whether they are published or not. The documents may come from teaching and research institutions in France or abroad, or from public or private research centers.

L'archive ouverte pluridisciplinaire **HAL**, est destinée au dépôt et à la diffusion de documents scientifiques de niveau recherche, publiés ou non, émanant des établissements d'enseignement et de recherche français ou étrangers, des laboratoires publics ou privés.

## RESEARCH ARTICLE

10.1029/2019AV000155

## Key Points:

- The monthly variability of deep convective organization in the tropics is investigated using satellite observations
- An enhanced organization of deep convection is associated with a drier troposphere, fewer high clouds, and a radiative cooling of the tropics
- Observations suggest equal and complementary modulations of the tropical radiation budget by convective organization and low-level stability

## Supporting Information:

- Supporting Information S1
- Original Version of Manuscript
- Peer Review History
- Authors' Response to Peer Review Comments
- First Revision of Manuscript
- Authors' Response to Peer Review Comments
- Second Revision of Manuscript [Accepted]

## Correspondence to:

S. Bony,  
sandrine.bony@lmd.jussieu.fr

## Citation:

Bony, S., Semie, A., Kramer, R. J., Soden, B., Tompkins, A. M., & Emanuel, K. A. (2020). Observed modulation of the tropical radiation budget by deep convective organization and lower-tropospheric stability. *AGU Advances*, 1, e2019AV000155. <https://doi.org/10.1029/2019AV000155>

Received 13 DEC 2019

Accepted 29 MAY 2020

Accepted article online 20 JUL 2020

**Peer Review** The peer review history for this article is available as a PDF in the Supporting Information.

©2020. The Authors.

This is an open access article under the terms of the Creative Commons Attribution License, which permits use, distribution and reproduction in any medium, provided the original work is properly cited.

# Observed Modulation of the Tropical Radiation Budget by Deep Convective Organization and Lower-Tropospheric Stability

S. Bony<sup>1</sup>, A. Semie<sup>1,2</sup>, R. J. Kramer<sup>3,4</sup>, B. Soden<sup>5</sup>, A. M. Tompkins<sup>6</sup>, and K. A. Emanuel<sup>7</sup>

<sup>1</sup>LMD/IPSL, Sorbonne University, CNRS, Paris, France, <sup>2</sup>Computational Data Science Program, Addis Ababa University, Addis Ababa, Ethiopia, <sup>3</sup>Climate and Radiation Laboratory, NASA Goddard Space Flight Center, Greenbelt, MD, USA, <sup>4</sup>Universities Space Research Association, Columbia, MD, USA, <sup>5</sup>RSMAS, University of Miami, Miami, FL, USA, <sup>6</sup>ICTP, Trieste, Italy, <sup>7</sup>Department of Earth, Atmospheric and Planetary Science, Massachusetts Institute of Technology, Cambridge, MA, USA

This study analyzes the observed monthly deseasonalized and detrended variability of the tropical radiation budget and suggests that variations of the lower-tropospheric stability and of the spatial organization of deep convection both strongly contribute to this variability. Satellite observations show that on average over the tropical belt, when deep convection is more aggregated, the free troposphere is drier, the deep convective cloud coverage is less extensive, and the emission of heat to space is increased; an enhanced aggregation of deep convection is thus associated with a radiative cooling of the tropics. An increase of the tropical-mean lower-tropospheric stability is also coincident with a radiative cooling of the tropics, primarily because it is associated with more marine low clouds and an enhanced reflection of solar radiation, although the free-tropospheric drying also contributes to the cooling. The contributions of convective aggregation and lower-tropospheric stability to the modulation of the radiation budget are complementary, largely independent of each other, and equally strong. Together, they account for more than sixty percent of the variance of the tropical radiation budget. Satellite observations are thus consistent with the suggestion from modeling studies that the spatial organization of deep convection substantially influences the radiative balance of the Earth. This emphasizes the importance of understanding the factors that control convective organization and lower-tropospheric stability variations, and the need to monitor their changes as the climate warms.

**Plain Language Summary** Anomalies of the tropically averaged radiative balance determine the time variations of the tropical climate. The stability of the lower atmosphere has been shown to influence this balance because increased stability favors the formation of low-level clouds and the reflection of solar radiation to space. Modeling studies have suggested that the spatial distribution of deep convection, especially the degree of clustering of deep clouds, could also impact humidity and cloud coverage, and thus the radiative balance of the Earth system. However, the relationships between cloud clustering, humidity, and the radiation budget have never been observed at the scale of the tropics. By analyzing long time series of satellite observations, we show that monthly variations of lower-atmospheric stability and convective clustering are both strongly correlated with variations of the radiative cooling of the tropics and that their contributions to the modulation of the radiation budget are complementary and equally important. These observational results thus confirm modeling inferences and emphasize that to predict the future of our climate, it will be necessary to determine how the stability and the clustering of deep convection will change with warming.

## 1. Introduction

How well do we understand the factors that modulate the tropical radiation budget? This understanding has long been recognized as a path toward interpreting the long-term stability of tropical temperatures over the past million years (Herbert et al., 2010) and estimating the sensitivity of the climate system to current and future increases of greenhouse gases in the atmosphere (Pierrehumbert, 1995). Observations and climate models suggest that the Earth's radiation budget is significantly influenced by changes in lower-tropospheric stability (Andrews & Webb, 2018; Ceppi & Gregory, 2017, 2019). An enhanced stability is associated with a strengthening of the inversion at the top of the marine boundary layer (Klein &

Hartmann, 1993; Wood & Bretherton, 2006), which reduces the mixing across the inversion and helps trap moisture at low levels. This favors the formation of low-level clouds, and thus the cooling of climate through the enhanced reflection of solar radiation.

More recently, modeling studies have hypothesized that variations in the spatial organization of deep convection could also influence the radiation balance of the Earth (Khairoutdinov & Emanuel, 2010; Mauritsen & Stevens, 2015): Idealized experiments have shown that when a randomly organized convection spontaneously organizes into dry and moist patches, on average the atmosphere becomes drier, clearer, and more efficient at emitting heat to space (Bretherton et al., 2005; Emanuel et al., 2014; Wing & Emanuel, 2014; Wing et al., 2017). The analysis of satellite observations has confirmed that for given conditions of large-scale circulation and surface temperature at the regional scale, situations associated with an enhanced convective aggregation are associated with decreased humidity, decreased upper-level cloudiness, increased outgoing longwave radiation (OLR), and decreased planetary albedo (Holloway et al., 2017; Stein et al., 2017; Tobin et al., 2012, 2013). However, these relationships might be affected by variations of sea surface temperatures (SSTs) and large-scale atmospheric circulations (Fueglistaler, 2019; Zhang & Fueglistaler, 2019). It also remains an open issue as to whether the radiative influence of changes in convective aggregation is significant compared to that of other well-established controlling factors such as the lower tropospheric stability.

In this study, we address these questions by analyzing observed variations of convective organization, tropospheric stability, and top-of-atmosphere (TOA) radiation budget over the tropical belt (30°S to 30°N) at the monthly time scale (once deseasonalized, the monthly tropical-mean radiation budget varies by  $\pm 1 \text{ Wm}^2$ ). First, we characterize the variability of the spatial organization of deep convection across the tropics, and we show that anomalies of convective organization strongly correlate with anomalies of tropospheric humidity and TOA radiation. We then show that convective organization and lower-tropospheric stability both exhibit strong anticorrelations to net radiation, through complementary influences. The relative influences of convective organization and stability on the tropical-mean radiation budget are further quantified and analyzed through radiative computations, and the implications of these results for climate change are discussed.

## 2. Data and Method

### 2.1. Convective Organization Index

To characterize the spatial organization of deep convection across the tropics, we use 3-hourly, intercalibrated and gridded infrared brightness temperature data  $T_b$  derived from geostationary satellites, a data set known as the GridSat-B1 data set (Knapp et al., 2011).  $T_b$  data are mapped on an equal-angle grid of  $0.07^\circ$ . The GridSat infrared calibration uncertainty is less than 0.5 K for each satellite, and the temporal uncertainty is less than 0.1 K per decade. We use data over the 30°S to 30°N latitude belt during the January 1990 to December 2017 period.

First, we detect the areas of the tropics covered by deep convection. To each 3-hourly snapshot distribution of  $T_b$  data we apply a smoothing of the  $T_b$  field using an exponential-distance decay over  $10 \times 10$  GridSat pixels (i.e., over a scale of about 80 km) to remove isolated convective pixels. Then, using the smoothed field, all local minima pixels are identified where the value of  $T_b$  is lower than that of the surrounding  $3 \times 3$  GridSat pixels. All local minima with  $T_b < 240 \text{ K}$  are considered to be deep convective centroids. The deep convective points detected through this “local minimum” method effectively detect organized convective features such as squall lines inferred from ground-based radar observations (see supporting information Figure S1 or Semie & Bony, 2020).

A close examination of the data reveals that some 3-hourly GridSat images exhibit an anomalously high number of undefined data (due, for instance, to the absence of a geostationary satellite), some anomalously low  $T_b$  values, or some spatial discontinuity near the edge of the satellite field of view due to the alternate use of nadirmost and second nadirmost satellite observations. To ensure a good homogeneity of the data over the whole tropical belt at any given time, we exclude the 3-hourly data for which more than 1% of the tropics are covered by undefined data, or for which the total number of deep convective centroids exceeds the long-term mean by more than two standard deviations. This represents 6% of all images over the 1990–2017 period, and less than 5% over the 2001–2017 period.

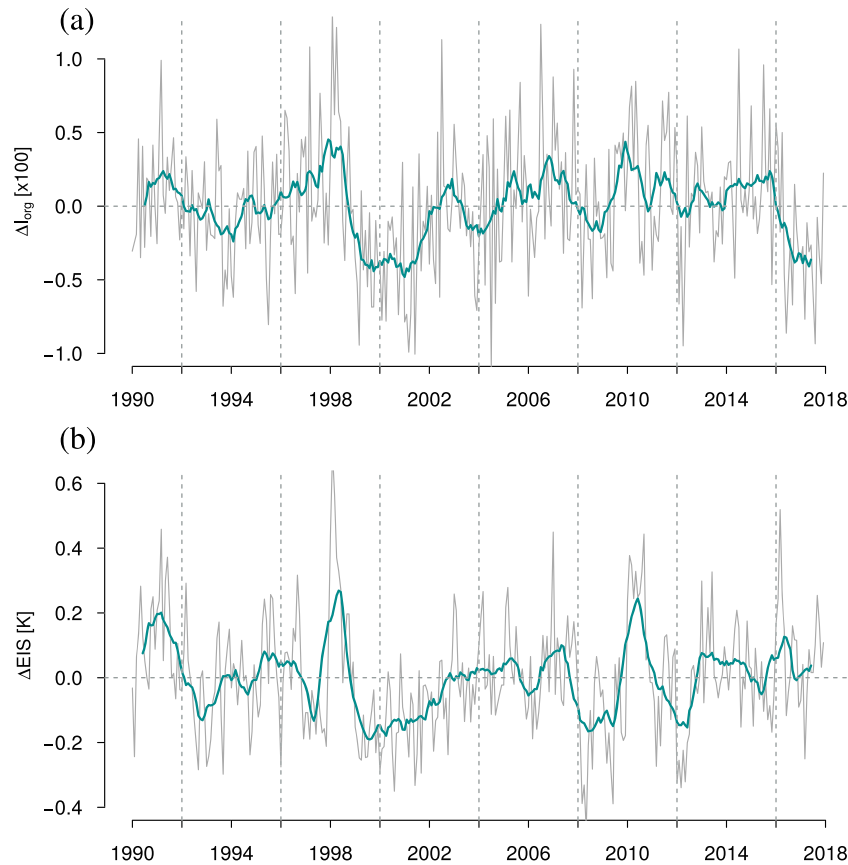


**Figure 1.** Time series of monthly deseasonalized and detrended anomalies of (a) the deep convective organization index  $I_{org}$  ( $\Delta I_{org}$ ) and (b) the tropical-mean lower-tropospheric stability EIS ( $\Delta EIS$ ). Gray lines show monthly anomalies, and green lines show 12-month running mean anomalies. The correlation coefficient between the monthly series of  $I_{org}$  and EIS is 0.4.

Then, we characterize the spatial organization of the deepest convective entities across the tropical belt (30°S to 30°N). For this purpose we use the  $I_{org}$  index, which has been originally introduced to characterize the degree of convective aggregation in cloud-resolving simulations (Tompkins & Semie, 2017) and has the advantage of characterizing the spatial organization relative to the reference of random organization at all spatial scales. This index compares the cumulative density function of the nearest-neighbor distances between deep convective centroids (NNCDF) to that expected for a random distribution of the same number of convective centroids. In the case of a random distribution associated with a Poisson process, the NNCDF is given by a Weibull distribution (Weger et al., 1992). Values of  $I_{org}$  significantly larger than 0.5 correspond to a clustered distribution, and the higher the value of  $I_{org}$ , the more aggregated the deep convective entities. The monthly anomalies of deep convective aggregation ( $\Delta I_{org}$ ) are given from the monthly averages of 3-hourly  $I_{org}$  values, deseasonalized, and with the linear trend removed (Figure S3 in the supporting information). Their time evolution is shown in Figure 1a.

To test the robustness of our characterization of the convective clustering, we alternatively calculated  $I_{org}$  using a different definition of convective centroids. Instead of defining them as the local minima of the smoothed  $T_b$  field within a  $3 \times 3$  pixels ( $0.21 \times 0.21^\circ$ ) domain, we apply a recursive clustering algorithm to the raw  $T_b$  field to identify convective “clusters” of adjoining pixels with  $T_b < 240$  K.  $I_{org}$  is then calculated from the nearest-neighbor distance between the centers of mass (centroid) of the deep convective clusters. The main difference with the local minima method is that only one centroid corresponds to each cluster of deep convection irrespective of the cluster size, significantly reducing the number of deep convective entities in areas where deep convective clusters are large. Although the method of local minima is

thought to better characterize the aggregation of deep convection than this clustering method, the interannual time series of  $I_{org}$  computed with the two methods are highly correlated ( $R = 0.9$ ) and the main conclusions of this study are similar for both methods (Table S1 and Figure S6 in the supporting information).

## 2.2. Lower-Tropospheric Stability

Previous studies (e.g., Ceppi & Gregory, 2017) have shown that the Earth's radiation budget is correlated to changes in lower-tropospheric stability and estimated inversion strength (EIS). These are defined as  $LTS = \theta_{700} - \theta_{1000}$ , where  $\theta_{700}$  and  $\theta_{1000}$  are potential temperatures at 700- and 1,000-hPa levels (Klein & Hartmann, 1993), and  $EIS = LTS - \Gamma_m^{850} (z_{700} - LCL)$  where  $\Gamma_m^{850}$  is the moist-adiabatic potential temperature gradient at 850 hPa,  $z_{700}$  is the height of the 700-hPa level, and  $LCL$  is the height of the lifting condensation level assuming a surface relative humidity of 80% (Wood & Bretherton, 2006).

To estimate these quantities, we use ERA-interim reanalyses at a spatial resolution of  $0.75^\circ$  in longitude and latitude (Dee et al., 2011). We compute EIS over each ocean region and compute the tropical-mean EIS as the spatial average over all tropical oceans ( $30^\circ\text{S}$  to  $30^\circ\text{N}$ ). The time evolution of deseasonalized and detrended anomalies of EIS ( $\Delta EIS$ ) is shown in Figure 1b.

## 2.3. Radiative Kernels

We use the radiative kernel technique to decompose the TOA radiative flux anomalies into contributions from changes in temperature, water vapor, surface albedo, and clouds (Soden & Held, 2006). To do so, we use anomalies of monthly-mean temperature and water vapor profiles from 2003 to 2014 from the Atmospheric Infrared Sounder (Aumann et al., 2003) Version 6 Level 3 product. Anomalies in surface albedo and cloud radiative effects are calculated using Clouds and Earth's Radiant Energy Systems Energy Balanced and Filled (CERES-EBAF) radiative fluxes for the same period of record. All anomalies are calculated relative to the mean over the whole period and the time series are deseasonalized and detrended.

To convert changes in the noncloud variables to a radiative response, we multiply each time series of anomalies by radiative kernels derived from CloudSat/CALIPSO observations (Kramer et al., 2019). Following common practice, we separately diagnose radiative responses due to uniform temperature change (Planck effect) and due to departures from the uniform temperature change (lapse rate response). Furthermore, since convective aggregation is associated with variability in middle- and upper-tropospheric relative humidity (e.g., Holloway et al., 2017), it is appropriate to decompose the water vapor radiative response into contributions from fixed and changing relative humidity. Following similar decompositions by Soden et al. (2008) and Held and Shell (2012), the fixed relative humidity radiative response is calculated by multiplying the water vapor radiative kernel by the planck and lapse rate components of total temperature change. We add these terms to the traditional planck and lapse rate radiative responses, respectively. The radiative response due to relative humidity changes is calculated by differencing the total water vapor and fixed relative humidity radiative responses. Due to nonlinear radiative responses to overlapping clouds, there is no radiative kernel specific to cloud perturbations in this methodology. Cloud radiative responses are therefore diagnosed from changes in cloud radiative effects corrected for cloud masking using the kernel-derived, noncloud radiative responses. Soden et al. (2008) outlines this approach in greater detail.

## 3. Variability of Deep Convective Organization

The computation of the  $I_{org}$  index for each 3-hourly image of the GridSat data set shows that, at the scale of the whole tropics ( $30^\circ\text{S}$  to  $30^\circ\text{N}$ ) and on average over the period 1990–2017, the distribution of deep convection is highly “clustered” (the mean  $I_{org}$  value is 0.82); that is, the deep convective centroids are closer to each other than would be predicted for a random distribution of the same number of centroids (Figures 2a and 2b).

The organization index computed over the  $30^\circ\text{S}$  to  $30^\circ\text{N}$ ,  $20^\circ\text{S}$  to  $20^\circ\text{N}$ , or  $15^\circ\text{S}$  to  $15^\circ\text{N}$  latitude bands (referred to as  $I_{org}$ ,  $I_{org}^{20}$ , and  $I_{org}^{15}$ , respectively) are highly correlated to each other ( $R = 0.92$  between  $I_{org}$  and  $I_{org}^{20}$ , and  $R = 0.85$  between  $I_{org}$  and  $I_{org}^{15}$ ). Therefore, although deep convection can sometimes happen at subtropical latitudes as a result of tropical wave activity or extratropical intrusions, the time variations of  $I_{org}$  computed over  $30^\circ\text{S}$  to  $30^\circ\text{N}$  are dominated by the variations of convective organization that occur at equatorial latitudes.

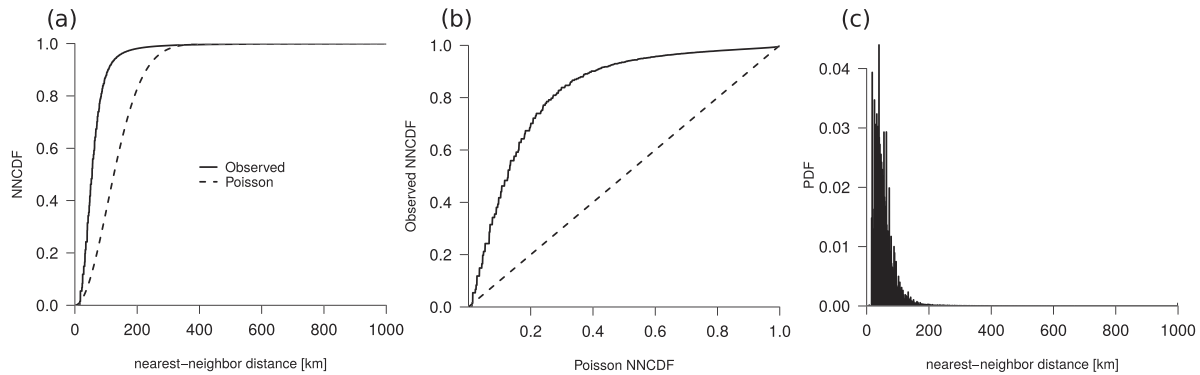


**Figure 2.** (a) Observed NNCDF (nearest-neighbor distances cumulative distribution function) of deep convective centroids across the tropical belt (solid line) compared to the NNCDF that would be theoretically expected for a random distribution of the same number of convective centroids (dashed line). (b) Relationship between the observed and Poisson NNCDFs (the convective organization index  $I_{org}$  corresponds to the area under the solid curve). (c) Probability distribution function of the nearest-neighbor distances among the observed deep convective centroids over the tropical belt. The distributions shown here are averaged over the 2001–2017 period, but qualitatively similar distributions are obtained when considering individual 3-hourly images (examples of instantaneous distributions are given in supporting information Figure S2).

Across the tropical belt, deep convection exhibits multiple spatial scales of organization, ranging from the planetary scale to the mesoscale. As  $I_{org}$  is a metric of spatial organization integrated across these multiple scales, one may wonder whether its variations are dominated by particular spatial scales. The  $I_{org}$  index is based on the distribution of nearest-neighbor distances across the tropics. The probability distribution function of nearest-neighbor distances shows that 98% of these distances are shorter than 200 km (Figure 2c). Therefore, although  $I_{org}$  characterizes the spatial organization of deep convection over a large range of scales, in practice, most of the variability of the deep convective organization captured by  $I_{org}$  arises from the mesoscale or, to be precise, from what Orlanski (1975) calls the meso- $\beta$  (20 to 200 km) scale.

The spatial organization of deep convection observed during 1990–2017 varies on a range of timescales. A spectral analysis of 3-hourly data shows that diurnal and semiannual variations constitute the dominant modes of variability (not shown). Those modes of variability forced by the variations of the insolation are removed when  $I_{org}$  is averaged over the day and the mean seasonal cycle of the daily-mean values is subtracted. The time series of the diurnally averaged and deseasonalized  $I_{org}$  then exhibits prominent modes of variability at intraseasonal and interannual time scales (Figure 3). Part of the intraseasonal variability relates to Madden-Julian Oscillations (Madden & Julian, 1994), whose timescale is around 30–60 days,

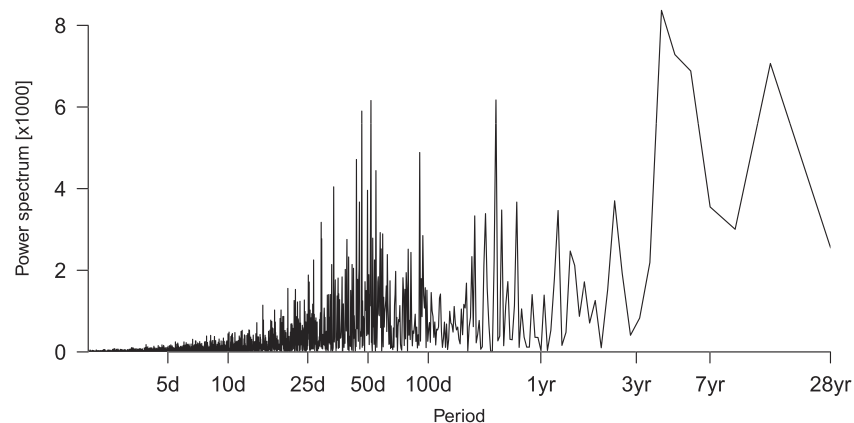


**Figure 3.** Power spectrum of daily-mean, deseasonalized and detrended data of the deep convective organization index  $I_{org}$  computed within 30°S to 30°N over the 1990–2017 period.



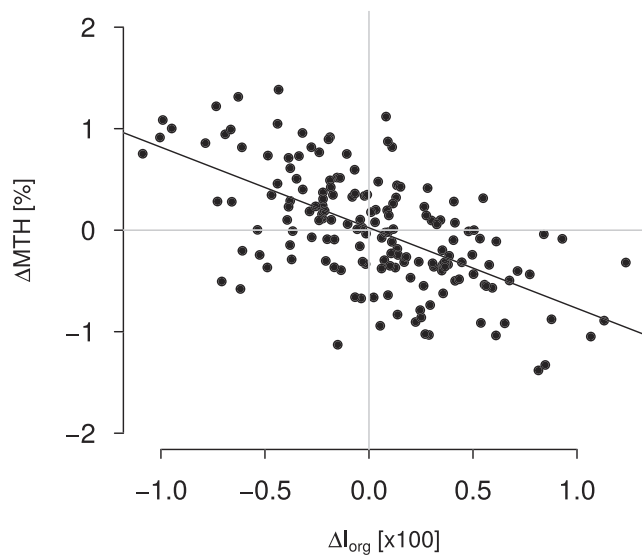


**Figure 4.** Relationship between monthly deseasonalized and detrended anomalies of the tropically averaged midtropospheric relative humidity (MTH) derived from microwave satellite observations and anomalies of the deep convective organization index  $I_{org}$ . Each marker corresponds to 1 month of the 2001–2014 period. Also reported is the linear regression line across all points.

and part of the interannual variability relates to the El Niño–Southern Oscillation (ENSO), which is dominated by the 3- to 7-year timescale (Radel et al., 2016; Rasmusson & Carpenter, 1982) (*supporting information* Figure S10). These tropical phenomena are known to modulate the spatial distribution of deep convection at the planetary scale. The fact that  $I_{org}$  is based on nearest-neighbor distances smaller than 200 km (Figure 2c) suggests therefore that  $I_{org}$  reflects these planetary-scale modes of variability primarily through their impact on the mesoscale organization of convection that is embedded within the large-scale envelopes of deep convection (in the case of the MJO, this observation is at odds with Dias et al., 2017). Note that  $I_{org}$  anomalies are poorly correlated to anomalies of the tropical-mean SST, and they are only moderately correlated to the Southern Oscillation Index defined as the sea level pressure difference between Tahiti and Darwin (*supporting information* Table S1).

In the rest of this paper, we will focus on monthly deseasonalized and detrended anomalies of  $I_{org}$  computed within 30°S to 30°N, and of several atmospheric and radiative properties averaged over the same tropical belt. These monthly anomalies include interannual variations as well as some intraseasonal variations (a significant part of the  $I_{org}$  variance occurs around the 50-day timescale; Figure 3).

#### 4. Convective Organization, Water Vapor, and Radiation

How does convective organization relate to tropospheric humidity? Figure 4 shows that monthly anomalies of the tropical-mean midtropospheric relative humidity inferred from microwave satellite observations over the 1999–2014 period (Chung et al., 2013) are strongly anticorrelated ( $R = -0.63$ ) with  $I_{org}$  anomalies: As convective aggregation is stronger, the midtroposphere (300–700 hPa) is drier on average over the tropics.

Several factors can contribute to this anticorrelation. Cloud-resolving models suggesting that drier atmospheres can inhibit the development of deep convection (Tompkins, 2001), mean drying could be associated with a contraction of the convective areas, and depending on how the drying is manifested spatially, could influence the organization of deep convection. Dry anomalies in the free troposphere can also help trigger convective self-aggregation (Emanuel et al., 2014). In turn, the clustering of convection enhances the precipitation efficiency of convective systems (Bao & Sherwood, 2019; Tobin et al., 2012), promoting the drying of the atmosphere. While causal relationships are difficult to unravel from observations, the anticorrelation between convective aggregation and large-scale tropospheric humidity found in modeling studies (Bretherton et al., 2005; Wing & Cronin, 2016; Wing & Emanuel, 2014) is confirmed by observations when considering monthly variations at the scale of the tropics.

The regional pattern of humidity changes associated with aggregation variations is investigated by regressing the local anomalies of midtropospheric relative humidity onto  $I_{org}$  anomalies (Figure 5a): An increase of the organization of deep convection is associated with large areas of drying in equatorial regions and in the subtropics. An exception is the western Pacific warm pool which, on the contrary, is associated with an enhanced convective activity and a moistening of the troposphere when  $I_{org}$  increases. Upper-tropospheric relative humidity data show similar results (not shown).

The CERES-EBAF, Edition 4.0, observations (Loeb et al., 2018) make it possible to investigate the impact of this drying on monthly radiative fluxes at TOA. The drying associated with the enhanced organization of convection is associated with an enhanced emission of clear-sky longwave (LW) radiation to space (due to the lower effective emission height of infrared radiation), a reduced absorption of clear-sky shortwave (SW) radiation by water vapor molecules, and then an enhanced net clear-sky cooling at TOA. This is true on average over the tropics ( $R = -0.54$ ; Table 1), and locally over most of the tropics when clear-sky net radiation anomalies are regressed onto  $I_{org}$  anomalies (Figure 5b).

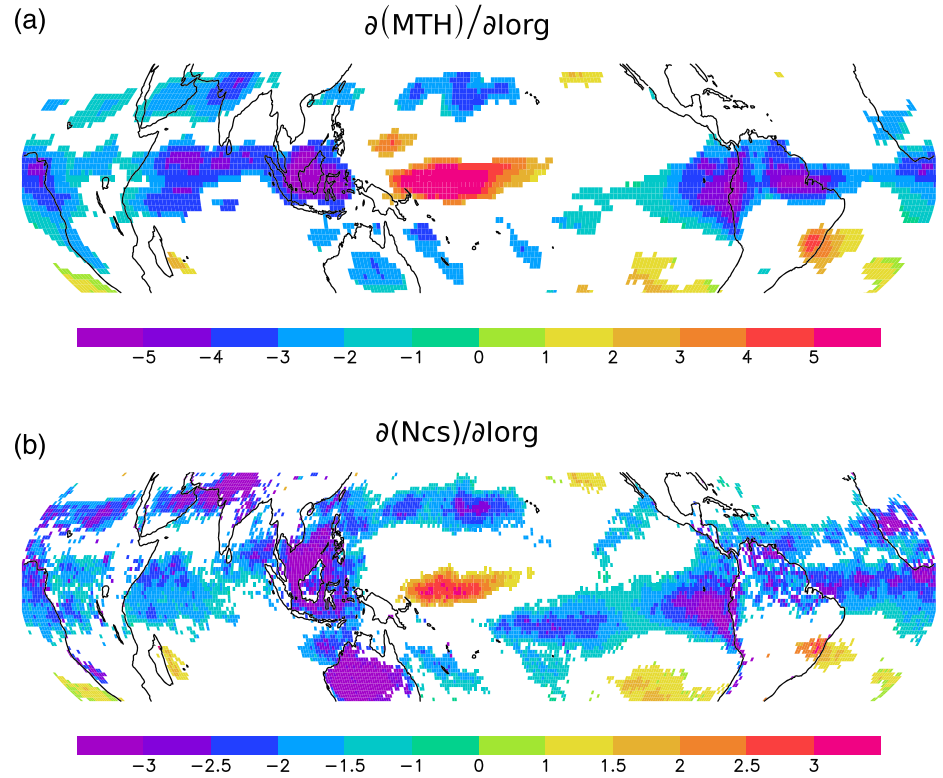


**Figure 5.** Linear regression onto  $I_{org}$  anomalies of regional monthly deseasonalized and detrended anomalies of (a) midtropospheric relative humidity (MTH) and (b) clear-sky net radiation  $N_{CS}$  ( $\partial MTH/\partial I_{org}$  and  $\partial N_{CS}/\partial I_{org}$ , respectively). MTH units are %,  $N_{CS}$  is in  $Wm^2$ , and  $I_{org}$  is dimensionless. Results are reported where the regional relationship is statistically significant ( $p$  value lower than 0.05).

The radiative cooling associated with positive anomalies of deep convective organization does not only occur in clear-sky but also in all-sky conditions (Table 1). The tropically averaged net radiation budget  $N$  is anticorrelated with  $I_{org}$  variations ( $R = -0.65$ ; Figure 6a), mostly through its LW component. This partly results from the drying of the atmosphere and its impact on clear-sky radiation and also from the reduced LW cloud radiative effects ( $CRE_{lw}$ , the difference between TOA clear-sky and all-sky outgoing radiative fluxes). It is explained by the fact that an increase of convective organization is associated with a reduced area of deep convection and, as shown by cloud observations from the spaceborne lidar CALIPSO (Chepfer et al., 2010), with a reduced high-level cloud amount (supporting information Figure S4 and Table S2).

## 5. Convective Organization Versus Lower-Tropospheric Stability

As  $I_{org}$ , EIS exhibits variability over the 1990–2017 period (Figure 1b), and monthly anomalies of EIS are strongly anticorrelated with  $N$  anomalies ( $R = -0.66$ ; Figure 6b and Table 1). Cloud observations show that this occurs mostly through the cloudy component of  $N$ , and more specifically through the albedo effect of clouds ( $CRE_{sw}$ ) which strengthens when EIS, and thus low-level clouds, increase (supporting information Table S2). However, as will be discussed later, we also note a negative correlation between anomalies of  $N_{cs,lw}$  and EIS, as strong as that between  $N_{cs,lw}$  and  $I_{org}$ .

In contrast to EIS or  $I_{org}$ , the tropical-mean SST is only weakly correlated with  $N$  variations ( $R = -0.16$ ), and it does not exhibit any significant correlation to  $I_{org}$  and EIS variations. The occurrence of El Niño/La Niña events is also found to have a minor effect on the relationships described here (supporting information Table S3). Therefore, although these events modulate  $I_{org}$  and EIS, they do not seem to affect the relationships between  $I_{org}$  (or EIS) and clouds or humidity in a specific way.



**Table 1**

Linear Correlation Coefficients of the Different Components of the Net Radiation Budget ( $N$ , with  $N = N_{cs} + CRE$ , Where  $N_{cs} = N_{cs,lw} + N_{cs,sw}$ ;  $N_{cs,lw} = -OLR_{cs}$  and  $CRE = CRE_{lw} + CRE_{sw}$ ,  $CS$  Referring to as “Clear-Sky” and  $CRE$  “Cloud Radiative Effect”) and of the Midtropospheric Relative Humidity (MTH) with the Deep Convective Organization Index  $I_{org}$  and the Lower-Tropospheric Stability EIS

	$N$	$N_{cs}$	$CRE$	$N_{lw}$	$N_{sw}$	$N_{cs,lw}$	$N_{cs,sw}$	$CRE_{lw}$	$CRE_{sw}$	MTH
$I_{org}$	−0.65	−0.54	−0.43	−0.53	−0.22	−0.47	−0.33	−0.39	(−0.13)	−0.63
EIS	−0.66	−0.44	−0.55	−0.36	−0.41	−0.47	(−0.10)	(−0.09)	−0.41	−0.56

Note. All quantities are tropical monthly means (note that EIS is averaged over ocean only), and correlations are calculated on the basis of monthly deseasonalized and detrended anomalies over 2001–2017 (1999–2014 for correlations with MTH). Coefficients in brackets are not statistically significant ( $p$  value larger than 0.05).

The tropical-mean radiation budget thus exhibits strong anticorrelations with both EIS and the organization of deep convection ( $R = -0.66$  and  $-0.65$ , respectively), each explaining about 40% of its variance.  $I_{org}$  and EIS are positively correlated to each other ( $R = 0.37$  during 2001–2017), but they correlate to the radiation budget through different ways, with  $I_{org}$  primarily affecting the clear-sky component and EIS primarily the cloudy component (Table 1). This suggests that  $I_{org}$  and EIS exert complementary influences on  $N$ . This is confirmed by Figure 6c, which shows how  $N$  anomalies ( $\Delta N$ ) relate to  $I_{org}$  and EIS anomalies ( $\Delta I_{org}$  and  $\Delta EIS$ , respectively). Negative  $\Delta N$  tend to be associated with both positive  $\Delta I_{org}$  and positive  $\Delta EIS$ , but the anticorrelation between  $\Delta I_{org}$  and  $\Delta N$  remains for a given  $\Delta EIS$ , and the anticorrelation between  $\Delta EIS$  and  $\Delta N$  remains for a given  $\Delta I_{org}$ . This is consistent with the partial correlations  $R(N, I_{org})_{EIS}$  and  $R(N, EIS)_{I_{org}}$ , which are equal to  $-0.58$  and  $-0.60$ , respectively.

Note that the anticorrelation of  $\Delta N$  with  $\Delta I_{org}$  and  $\Delta EIS$  is not only found at the monthly timescale but also, to a lesser extent, at the daily timescale (Figure S7 in the supporting information), showing the robustness of the relationships between  $N$ ,  $I_{org}$ , and EIS.

Given the complementary influences of  $I_{org}$  and EIS on  $N$ , we assess the ability of  $\Delta I_{org}$  and  $\Delta EIS$  to predict  $\Delta N$ . A linear multiple regression calculation shows that the simple model  $\Delta N = \alpha \Delta I_{org} + \beta \Delta EIS$  with  $(\alpha, \beta) = (-111.41 \text{ Wm}^2, -3.14 \text{ Wm}^2 \text{ K}^{-1})$  explains more than 60% of the variance of monthly  $N$  anomalies (Figure 7a;  $R = 0.79$ ,  $R^2 = 0.62$ ), that is, much more than that explained (about 40%) by either  $\Delta I_{org}$  or  $\Delta EIS$  individually. When considering low-pass-filtered anomalies (6-month running mean), the simple model explains almost 75% of the variance ( $R = 0.86$ ,  $R^2 = 0.74$ ). The multiplication of  $\alpha$  and  $\beta$  by the variances of  $\Delta I_{org}$  and  $\Delta EIS$  over the 2001–2017 period ( $\sigma_{I_{org}} = 4.3 \times 10^{-3}$  and  $\sigma_{EIS} = 0.16 \text{ K}$ ) reveals the relative influence of  $I_{org}$  and EIS variations on  $N$  variations. As  $\alpha \sigma_{I_{org}} = -0.48 \text{ Wm}^2$  and  $\beta \sigma_{EIS} = -0.50 \text{ Wm}^2$ , the influences of  $I_{org}$  and EIS on  $N$  variations appear to be of similar order of magnitude.

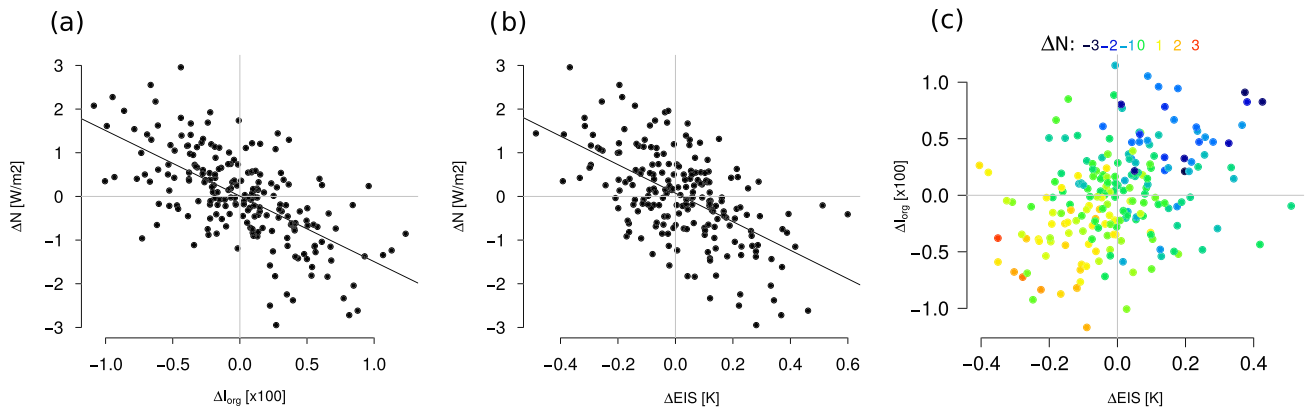


**Figure 6.** Monthly anomalies of the observed tropically averaged Earth radiation budget  $\Delta N$  versus anomalies of (a) the organization index of deep convection  $\Delta I_{org}$  or (b) lower-tropospheric stability (EIS) averaged over tropical ocean  $\Delta EIS$ . (c)  $\Delta N$  anomalies (in color) stratified by  $\Delta I_{org}$  and  $\Delta EIS$ . Each point corresponds to 1 month of the 2001–2017 period (all anomalies are deseasonalized and detrended).

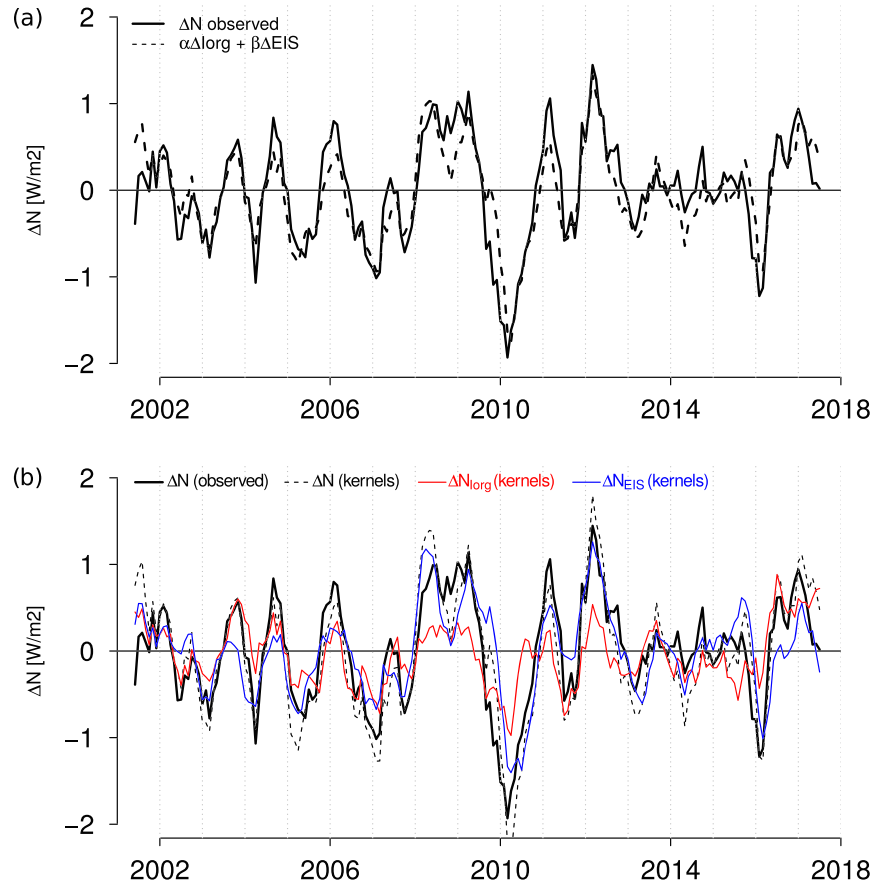


**Figure 7.** (a) Time series of monthly deseasonalized and detrended anomalies of the tropically averaged Earth radiation budget  $\Delta N$  derived from CERES satellite observations (thick solid line) and reconstituted (dashed line) from  $\Delta I_{org}$  and  $\Delta EIS$  through linear multiple regression ( $\Delta N = \alpha \Delta I_{org} + \beta \Delta EIS$ ). (b) Time series of the tropical-mean  $\Delta N$  observed from CERES (thick solid line) and reconstructed from kernel radiative calculations (thin solid line; Equation 1). Also reported are the radiative contributions due to  $I_{org}$  anomalies (in red) and to EIS anomalies (in blue) inferred from kernel calculations (Kramer et al., 2019). Note that the two reconstitutions of  $\Delta N$  reported on panels (a) and (b) correspond to two distinct approximations: In (a) it is assumed that  $N$  depends only on  $I_{org}$  and EIS, while in (b) it is assumed that  $N$  can be reconstructed from the variations in temperature, humidity, etc., which are congruent with  $I_{org}$  and EIS variations. On both time series, a 6-month running mean has been applied (for the plotting only).

## 6. Decomposition of Radiative Anomalies

By using radiative kernels (Kramer et al., 2019; section 2.3), the total TOA flux anomalies can be decomposed into contributions from changes in temperature, water vapor, surface albedo, and clouds:

$$\Delta N = \sum_{x=T, RH, A} K_x \Delta x + \Delta N_C = \sum_{x=T, RH, A, C} \Delta N_x. \quad (1)$$

In this expression,  $K_x$  is the radiative kernel associated with temperature ( $T$ ), relative humidity ( $RH$ ), or surface albedo ( $A$ ) variations, and  $\Delta N_C$  is the contribution of cloud changes to  $\Delta N$ , computed as the change in cloud radiative effect corrected for cloud masking. This decomposition is applied regionally for each month, and each component of the decomposition is then regressed against the monthly time series of  $I_{org}$  and EIS anomalies (Table 2), so that Equation 1 can be rewritten as follows:

$$\Delta N = \sum_{x=T, RH, A, C} \left( \frac{\partial N_x}{\partial I_{org}} \Delta I_{org} + \frac{\partial N_x}{\partial EIS} \Delta EIS \right) = \Delta N_{I_{org}} + \Delta N_{EIS}, \quad (2)$$

where  $\Delta N_{I_{org}}$  and  $\Delta N_{EIS}$  represent the  $I_{org}$  and EIS contributions to  $\Delta N$ , respectively.

**Table 2**

Contributions of Changes in Temperature (Uniform and Lapse Rate Variations), Surface Albedo, Relative Humidity, and Clouds ( $\pm$  the 1–99% Confidence Interval) to the Tropical-Mean Radiative Responses to  $I_{org}$  and EIS

$x$	$\frac{\partial N_x}{\partial I_{org}} \sigma_{I_{org}}$ (W m $^{-2}$ )	$\frac{\partial N_x}{\partial EIS} \sigma_{EIS}$ (W m $^{-2}$ )	$R(N_x, I_{org})$	$R(N_x, EIS)$
$\Delta$ temperature (uniform, constant RH)	$-0.02 \pm 0.07$	$-0.06 \pm 0.06$	$-0.06$	$-0.21$
$\Delta$ temperature (lapse rate, constant RH)	<b><math>-0.11 \pm 0.05</math></b>	<b><math>-0.13 \pm 0.04</math></b>	<b><math>-0.44</math></b>	$-0.54$
$\Delta$ surface albedo	$0 \pm 0.02$	$0 \pm 0.02$	$0$	$0$
$\Delta$ relative humidity	<b><math>-0.20 \pm 0.07</math></b>	<b><math>-0.15 \pm 0.06</math></b>	<b><math>-0.56</math></b>	<b><math>-0.47</math></b>
$\Delta$ cloud (LW)	<b><math>-0.18 \pm 0.10</math></b>	$-0.03 \pm 0.09$	<b><math>-0.37</math></b>	$-0.07$
$\Delta$ cloud (SW)	$-0.15 \pm 0.16$	<b><math>-0.32 \pm 0.13</math></b>	$-0.20$	<b><math>-0.47</math></b>

*Note.* To facilitate the comparison between the different sensitivities, the sensitivities to  $I_{org}$  and EIS have been multiplied by the interannual standard deviation of  $I_{org}$  or EIS ( $\sigma_{I_{org}} = 4.3 \times 10^{-3}$  and  $\sigma_{EIS} = 0.16$  K, respectively). The values in bold are statistically significant ( $p$  value lower than 0.01). Also reported are correlation coefficients ( $R$ ) between monthly deseasonalized and detrended anomalies of  $N_x$  and  $I_{org}$  or EIS.

The  $N$  anomalies reconstructed from kernel calculations (using Equation 2) are shown in Figure 7b together with the  $\Delta N$  actually observed and the radiative contributions of convective organization and lower-tropospheric static stability to these anomalies. The observed and reconstructed  $\Delta N$  exhibit the same good agreement ( $R = 0.79$ ) as seen in Figure 7a. Although the EIS contribution dominates  $\Delta N$  during ENSO years, most of the time,  $I_{org}$  and EIS contributions are of same order of magnitude.

The radiative responses to  $I_{org}$  and EIS are mainly driven by variations in relative humidity and cloudiness (Table 2).  $\Delta N_{I_{org}}$  arises as much from changes in relative humidity as from changes in LW cloud radiative effects, with an additional contribution from lapse rate variations, while  $\Delta N_{EIS}$  arises primarily from SW cloud radiative effects, with an additional contribution from relative humidity and lapse rate variations.

More surprisingly, relative humidity changes appear to contribute to  $\Delta N$  as much through  $I_{org}$  variations ( $-0.20$  W m $^{-2}$ ) as through EIS variations ( $-0.15$  W m $^{-2}$ ). Similarities are also found when considering the zonally averaged vertical distribution of  $\Delta N_{RH}$  regressed onto  $I_{org}$  or EIS variations (Figure 8). As discussed earlier, an increase in convective organization or in EIS is associated with a drying of the free troposphere over most of the tropical belt (Table 1) and leads to a net radiative cooling at TOA. Figure 8 shows that this

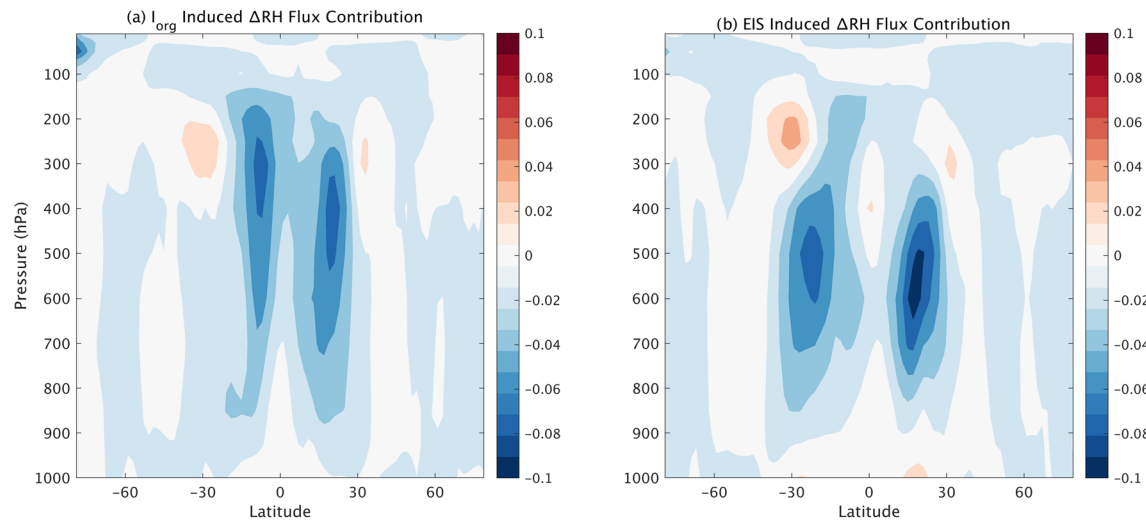


**Figure 8.** Sensitivity to (a)  $I_{org}$  and (b) EIS variations of the radiative response to changes in relative humidity at each atmospheric level calculated through the kernel approach, multiplied by the interannual standard deviation of  $I_{org}$  or EIS ( $\sigma_{I_{org}} = 4.3 \times 10^{-3}$  and  $\sigma_{EIS} = 0.16$  K, respectively). Units: W m $^{-2}$  (100 hPa) $^{-1}$ . The tropically averaged, vertical integrals of each panel correspond to the relative humidity contributions  $\frac{\partial N_{RH}}{\partial I_{org}} \sigma_{I_{org}}$  and  $\frac{\partial N_{RH}}{\partial EIS} \sigma_{EIS}$  (in W m $^{-2}$ , reported in Table 2), respectively.

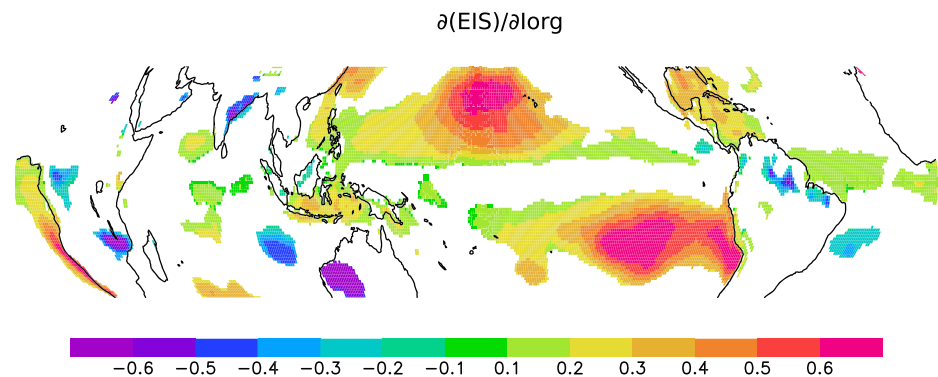


**Figure 9.** Regional monthly EIS anomalies (deseasonalized and detrended) regressed onto  $I_{org}$  anomalies during 2001–2017. Results are reported where the relationship is significant ( $p$  value lower than 0.05).

radiative cooling stems from the drying of the free troposphere over its whole depth, mostly in equatorial regions in the case of  $I_{org}$  variations, and mostly in subtropical regions in the case of EIS variations.

## 7. Summary and Discussion

This study suggests that monthly variations of the tropical radiation budget can be explained to a large extent by the radiative influences of variations in the lower-tropospheric stability and in the spatial organization of deep convection. Both influences are equally strong, and despite a modest correlation between convective organization and lower-tropospheric stability, largely independent of each other. Observations also suggest that they are complementary because they operate on different components of the radiation budget; the clustering of deep convection affects TOA radiation mostly through its influence on clear-sky radiation and LW CRE, which relate to variations of free-tropospheric relative humidity and high-level clouds, respectively. On the other hand, lower-tropospheric stability affects TOA radiation primarily through its influence on SW CRE, which relates to variations of low-level clouds.

Given the anticorrelation between convective organization and the deep convective area fraction (Figure S4), the question arises as to whether the relationship between convective organization and radiation might be simply explained by the relationship between the convective area fraction ( $f$ ) and radiation. However, the relationship between  $f$  and  $N$  is much weaker than that between  $I_{org}$  and  $N$  (correlations of 0.36 and  $-0.65$ , respectively), and the strong anticorrelation between  $I_{org}$  and  $N$  holds even in the absence of  $f$  variations (supporting information Figure S6). The relationship between  $I_{org}$  and  $N$  is thus not primarily explained by variations of the fractional area of the tropics covered by deep convection, but rather by variations in how deep convection is *spatially distributed* across the tropics.

Given the strong potential influence of convective organization and stability on the tropical radiation budget, it will be important to understand what drives their variations in present and future climates. One possible influencing factor in variations of  $I_{org}$  and/or EIS is the tropical large-scale overturning circulation.  $I_{org}$  and EIS anomalies are poorly correlated to basic metrics of this circulation, such as the mean subsidence fraction (the fractional area of the tropics covered by large-scale downward motions), the mean large-scale subsiding motion or the mean circulation strength, as diagnosed by Bony et al. (2013) using large-scale vertical velocity data from ERA-interim reanalyses. Nevertheless, compared to the lowest quartile, the highest quartile of the  $I_{org}$  distribution is associated with a larger subsidence fraction (by about 4%) and a strengthening of the overturning circulation (by about 8%), suggesting some relationship between convective organization and the large-scale tropical circulation (supporting information Figure S9).

Previous research has shown that on interannual, decadal, and longer time scales, EIS depends on the spatial pattern of surface temperatures, especially on the temperature difference between warm convective areas and the rest of the tropics (Ceppi & Gregory, 2017; Fueglistaler, 2019; Qu et al., 2015; Zhou et al., 2016). Monthly EIS anomalies are positively correlated ( $R = 0.54$ ) with anomalies of the SST<sup>#</sup> index proposed by Fueglistaler (2019) (defined as the surface temperature difference between the 30% warmest waters minus

the tropical average SST), thus suggesting that EIS variations are partly controlled by the spatial pattern of surface temperature. We also note a strong anticorrelation between EIS and relative humidity in the free troposphere (Table 1). This magnitude of anticorrelation does not exist between EIS and the area and/or strength of large-scale subsidence in the tropics. Therefore, we suggest that it arises rather from a radiative coupling: Dry anomalies in the free troposphere enhance the radiative cooling at the top of the moist boundary layer of subtropical regions, which strengthens the inversion at the top of the boundary layer and thus EIS. By inhibiting the vertical development of convective clouds, a stronger EIS prevents the free troposphere from being moistened by the detrainment of shallow or deeper congestus clouds, thus reinforcing the anticorrelation between MTH and EIS.

Since periods of enhanced convective organization are associated with dry anomalies in the mid and upper troposphere (Figure 5), they are likely to induce a positive correlation between convective organization and EIS anomalies. Indeed, the regression of regional EIS anomalies onto  $I_{org}$  anomalies shows a clear enhancement of EIS on both sides of equatorial regions when convective organization is stronger (Figure 9). This is consistent with the positive correlation between  $I_{org}$  and the tropical-mean EIS ( $R = 0.37$ ). This is also consistent with idealized modeling studies showing the interplay between deep convective organization and lower-tropospheric stability (Chen & Wu, 2019; Coppin & Bony, 2018).

The factors that control the spatial organization of deep convection across the tropics constitute an area of active research. Modeling studies suggest that the aggregation of deep convection strongly depends on atmospheric radiative processes (Holloway & Woolnough, 2016; Muller & Bony, 2015; Muller & Held, 2012; Wing & Emanuel, 2014), and on the spatial distribution of surface temperatures (Coppin & Bony, 2018). It may also be sensitive to the mean surface temperature (see Wing et al., 2017, for a review), although idealized simulations of the tropical atmosphere do not provide consistent results on that matter. Some modeling studies suggest that convective aggregation increases under global warming (Coppin & Bony, 2015; Pendergrass et al., 2016), but others suggest that conclusions regarding the sensitivity of convective organization to warming depend on the metric used to quantify the organization, and on the range of warming considered (Cronin & Wing, 2017). The present observational analysis is not more conclusive in that regard, as  $I_{org}$  does not exhibit any significant trend during 2001–2017, and indeed, the correlation between convective organization and the tropical-mean surface temperature is insignificant (*supporting information* Table S1). On the other hand, convective organization might be more sensitive to changes in regional SST patterns (Coppin & Bony, 2018; Zhang & Fueglistaler, 2019). Preliminary investigations suggest that  $I_{org}$  and EIS correlate to different SST patterns (*supporting information* Figure S8). Future investigations should thus determine how much the radiative influence of SST patterns, which partly results from the influence of the SST distribution on EIS (Zhou et al., 2016), also stems from the influence of SST patterns on the organization of deep convection. Future investigations should also determine how changes in convective organization at the tropical scale relate to changes in weather and convective organization at the regional scale, including their impact on extreme precipitation (Semie & Bony, 2020).

However, in addition to being potentially affected by slowly varying boundary conditions such as SST changes, the spatial organization of deep convection may also be affected by purely internal atmospheric variability. For instance,  $I_{org}$  exhibits some variability at timescales characteristic of the Madden-Julian Oscillation (Figure 3), which has been suggested to be a manifestation of an instability driven by cloud radiation feedbacks (Arnold & Randall, 2015; Emanuel et al., 2014; Khairoutdinov & Emanuel, 2018). This is in contrast with the lower-tropospheric stability, which does also exhibit variability at interannual timescales but not at the intraseasonal timescale (*supporting information* Figure S10). Therefore, while  $I_{org}$  and EIS might both be sensitive to slow changes in the ocean-atmosphere system,  $I_{org}$  presumably results as well from short-term processes and interactions within the atmosphere.

All the relationships discussed in this paper have been established on the basis of detrended time series. During the period 2001–2017,  $I_{org}$  exhibits a weak positive trend which is not statistically significant. On the other hand, EIS exhibits a clear positive trend (+0.17 K per decade), consistent with the larger warming of the atmosphere at altitude than near the surface (Qu et al., 2015). One may expect this increase of EIS to produce a negative trend of the tropical radiation budget, but we actually observe the opposite ( $N$  increases by  $0.35 \text{ W m}^{-2}$  per decade). The positive trend of  $N$  being dominated by its clear-sky component, it likely arises from the increase of greenhouse gas concentrations in the atmosphere, which increases the



absorption of clear-sky solar radiation and reduces the emission of clear-sky infrared radiation to space. Indeed, considering both  $I_{org}$ , EIS and the  $\text{CO}_2$  atmospheric concentration explains 63% of the variance and improves the reproduction of the trend.

How does the tropical radiation budget  $N$  relate to the global-mean radiation budget  $N_G$ ? Monthly deseasonalized variations of  $N$  and  $N_G$  are of same order of magnitude ( $\pm 1 \text{ W m}^{-2}$  and  $\pm 0.7 \text{ W m}^{-2}$ , respectively), are highly correlated to each other ( $R = 0.86$ ), and are both anticorrelated with the tropical  $I_{org}$  and EIS variations ( $R = -0.54$  and  $-0.56$ , respectively). Variations in  $I_{org}$  and EIS explain together 44% of the variance of the detrended  $N_G$  signal, and when considering the  $\text{CO}_2$  concentration as an additional predictor, nearly half (47%) of the variance of the trended signal can be explained (note that considering the global-mean near-surface temperature does not increase the percentage of variance explained because the surface temperature is poorly correlated with  $N_G$ ). Therefore, variations of deep convective organization and lower-tropospheric stability in the tropics are relevant not only for the tropical radiation budget but also for the global radiation balance.

Although the issue of whether and how convective organization and EIS will change in the future remains unsettled, this observational study suggests that their changes at decadal or longer time scales might matter for the radiation balance of the Earth, water vapor and cloud feedbacks, and thus climate sensitivity. It stresses the importance of testing the ability of numerical models of the climate system to reproduce the observed relationships analyzed in this study. A recent comparison of CERES observations with simulations from the latest generation of general circulation models with parameterized convection (Loeb et al., 2020) shows that when forced by observed SSTs, climate models reproduce the observed evolution of TOA LW or NET radiative fluxes less well than the evolution of TOA SW fluxes (when considering monthly deseasonalized anomalies, the correlation between simulations and observations ranges across models from 0.096 to 0.32 for  $N_{lw}$ , and from 0.25 to 0.38 for  $N$ ). Since in observations the variability of deep convective organization arises mostly from the mesoscale (section 3) and influences the radiation budget mostly in the LW (Table 1), the poor ability of climate models to reproduce observed monthly anomalies of  $N_{lw}$  might partly arise from their absence of representation of mesoscale convective organization.

Climate models might better reproduce low-frequency variations of  $N$  because of the reduced influence of stochastic atmospheric variability and the enhanced influence of surface boundary conditions (Proistosescu et al., 2018). However, in the event that long-term changes in surface boundary conditions or atmospheric composition would affect the mesoscale variability of deep convection, one would expect a biased prediction of climate sensitivity by models that do not predict the mesoscale organization of deep convection. It emphasizes therefore the need to better understand physically the factors that control convective organization, and the need to monitor their changes as the climate warms.

## Conflict of Interest

The author declares no conflicts of interest relevant to this study.

## Data Availability Statement

The GridSat-B1 data set is available at the NOAA National Centers for Environmental Information (NCEI, [www.ncdc.noaa.gov/gridsat/gridsat-index.php?name=data](http://www.ncdc.noaa.gov/gridsat/gridsat-index.php?name=data)), and the  $I_{org}$  time series is available at [doi.org/10.14768/20200420001.1](https://doi.org/10.14768/20200420001.1). ERA-interim reanalyses were downloaded from ClimServ ([climserv.ipsl.polytechnique.fr/fr/les-donnees/era-interim.html](http://climserv.ipsl.polytechnique.fr/fr/les-donnees/era-interim.html)). The EBAF Radiative Fluxes and Clouds data set (Edition 4A, [doi:10.5067/TERRA+AQUA/CERES/EBAF-TOA\\_L3B004.0](https://doi.org/10.5067/TERRA+AQUA/CERES/EBAF-TOA_L3B004.0)) is made available by the CERES group from the NASA Langley Research Center. CALIPSO-GOCCP data are available from [climserv.ipsl.polytechnique.fr/cfmip-obs/Calipso\\_goccp.html](http://climserv.ipsl.polytechnique.fr/cfmip-obs/Calipso_goccp.html) website. The Southern Oscillation Index (SOI) is available online ([www.cpc.ncep.noaa.gov/data/indices/soi](http://www.cpc.ncep.noaa.gov/data/indices/soi)).

## References

- Andrews, T., & Webb, M. J. (2018). The dependence of global cloud and lapse rate feedbacks on the spatial structure of tropical pacific warming. *Journal of Climate*, 31(2), 641–654. <https://doi.org/10.1175/JCLI-D-17-0087.1>
- Arnold, N. P., & Randall, D. A. (2015). Global-scale convective aggregation: Implications for the Madden-Julian Oscillation. *Journal of Advances in Modeling Earth Systems*, 7, 1499–1518. <https://doi.org/10.1002/2015MS000498>

## Acknowledgments

S. B. and A. S. are supported by the European Research Council (ERC) under the European Union's Horizon 2020 research program (Grant 694768). R. J. K. is supported by the NASA Postdoctoral Program, B. J. S. by NASA (Grant 80NSSC18K1032), and K. A. E. by the National Science Foundation (Grant NSF AGS-1906768). Paolo Ceppi, Stephan Fueglistaler, Tobias Becker, and an anonymous reviewer are thanked for their thoughtful and useful comments on the manuscript.

- Aumann, H. H., Chahine, M. T., Gautier, C., Goldberg, M. D., Kalnay, E., McMillin, L. M., et al. (2003). AIRS/AMSU/HSB on the Aqua mission: Design, science objectives, data products, and processing systems. *IEEE Transactions on Geoscience and Remote Sensing*, 41(2), 253–264. <https://doi.org/10.1109/TGRS.2002.808356>
- Bao, J., & Sherwood, S. C. (2019). The role of convective self-aggregation in extreme instantaneous versus daily precipitation. *Journal of Advances in Modeling Earth Systems*, 11, 19–33. <https://doi.org/10.1029/2018MS001503>
- Bony, S., Bellon, G., Klocke, D., Sherwood, S., Fermepin, S., & Denvil, S. (2013). Robust direct effect of carbon dioxide on tropical circulation and regional precipitation. *Nature Geoscience*, 6(6), 447–451. <https://doi.org/10.1038/NGEO1799>
- Bretherton, C. S., Bossey, P. N., & Khairoutdinov, M. (2005). An energy-balance analysis of deep convective self-aggregation above uniform SST. *Journal of the Atmospheric Sciences*, 62, 4273–4292. <https://doi.org/10.1175/JAS3614.1>
- Ceppi, P., & Gregory, J. M. (2017). Relationship of tropospheric stability to climate sensitivity and Earth's observed radiation budget. *Proceedings of the National Academy of Sciences of the United States of America*, 114(50), 13,126–13,131. <https://doi.org/10.1073/pnas.1714308114>
- Ceppi, P., & Gregory, J. M. (2019). A refined model for the Earth's global energy balance. *Climate Dynamics*, 53(7), 4781–4797. <https://doi.org/10.1007/s00382-019-04825-x>
- Chen, Y.-T., & Wu, C.-M. (2019). The role of interactive SST in the cloud-resolving simulations of aggregated convection. *Journal of Advances in Modeling Earth Systems*, 11, 3321–3340. <https://doi.org/10.1029/2019MS001762>
- Chepfer, H., Bony, S., Winker, D., Cesana, G., Dufresne, J. L., Minnis, P., et al. (2010). The GCM-Oriented CALIPSO Cloud Product (CALIPSO-GOCCP). *Journal of Geophysical Research*, 115, D00H16. <https://doi.org/10.1029/2009JD012251>
- Chung, E.-S., Soden, B. J., & John, V. O. (2013). Intercalibrating microwave satellite observations for monitoring long-term variations in upper- and midtropospheric water vapor. *Journal of Atmospheric and Oceanic Technology*, 30(10), 2303–2319. <https://doi.org/10.1175/JTECH-D-13-00001.1>
- Coppin, D., & Bony, S. (2015). Physical mechanisms controlling the initiation of convective self-aggregation in a general circulation model. *Journal of Advances in Modeling Earth Systems*, 7, 2060–2078. <https://doi.org/10.1002/2015MS000571>
- Coppin, D., & Bony, S. (2018). On the interplay between convective aggregation, surface temperature gradients, and climate sensitivity. *Journal of Advances in Modeling Earth Systems*, 10, 3123–3138. <https://doi.org/10.1029/2018MS001406>
- Cronin, T. W., & Wing, A. A. (2017). Clouds, circulation, and climate sensitivity in a radiative-convective equilibrium channel model. *Journal of Advances in Modeling Earth Systems*, 9, 2883–2905. <https://doi.org/10.1002/2017MS001111>
- Dee, D. P., Uppala, S. M., Simmons, A. J., Berrisford, P., Poli, P., Kobayashi, S., et al. (2011). The ERA-interim reanalysis: Configuration and performance of the data assimilation system. *Quarterly Journal of the Royal Meteorological Society*, 137(656), 553–597. <https://doi.org/10.1002/qj.828>
- Dias, J., Sakaeda, N., Kiladis, G. N., & Kikuchi, K. (2017). Influences of the MJO on the space-time organization of tropical convection. *Journal of Geophysical Research: Atmospheres*, 122, 8012–8032. <https://doi.org/10.1002/2017JD026526>
- Emanuel, K., Wing, A. A., & Vincent, E. M. (2014). Radiative-convective instability. *Journal of Advances in Modeling Earth Systems*, 6, 75–90. <https://doi.org/10.1002/2013MS000270>
- Fueglistaler, S. (2019). Observational evidence for two modes of coupling between sea surface temperatures, tropospheric temperature profile, and shortwave cloud radiative effect in the tropics. *Geophysical Research Letters*, 46, 9890–9898. <https://doi.org/10.1029/2019GL083990>
- Held, I. M., & Shell, K. M. (2012). Using relative humidity as a state variable in climate feedback analysis. *Journal of Climate*, 25(8), 2578–2582.
- Herbert, T. D., Peterson, L. C., Lawrence, K. T., & Liu, Z. (2010). Tropical ocean temperatures over the past 3.5 million years. *Science*, 328(5985), 1530–1534. <https://doi.org/10.1126/science.1185435>
- Holloway, C. E., Wing, A. A., Bony, S., Muller, C., Masunaga, H., L'Ecuyer, T. S., et al. (2017). Observing convective aggregation. *Surveys in Geophysics*, 38(6), 1199–1236. <https://doi.org/10.1007/s10712-017-9419-1>
- Holloway, C. E., & Woolnough, S. J. (2016). The sensitivity of convective aggregation to diabatic processes in idealized radiative-convective equilibrium simulations. *Journal of Advances in Modeling Earth Systems*, 8, 166–195. <https://doi.org/10.1002/2015MS000511>
- Khairoutdinov, M., & Emanuel, K. (2010). Aggregated convection and the regulation of tropical climate. In *29th Conference on Hurricanes and Tropical Meteorology*, pp. 2.69.
- Khairoutdinov, M., & Emanuel, K. (2018). Intraseasonal variability in a cloud-permitting near-global equatorial aquaplanet model. *Journal of the Atmospheric Sciences*, 75(12), 4337–4355. <https://doi.org/10.1175/JAS-D-18-0152.1>
- Klein, S. A., & Hartmann, D. L. (1993). The seasonal cycle of low stratiform clouds. *Journal of Climate*, 6(8), 1587–1606. [https://doi.org/10.1175/1520-0442\(1993\)006<1587:TSCOLS>2.0.CO;2](https://doi.org/10.1175/1520-0442(1993)006<1587:TSCOLS>2.0.CO;2)
- Knapp, K. R., Ansari, S., Bain, C. L., Bourassa, M. A., Dickinson, M. J., Funk, C., et al. (2011). Globally gridded satellite observations for climate studies. *Bulletin of the American Meteorological Society*, 92(7), 893–907. <https://doi.org/10.1175/2011BAMS3039.1>
- Kramer, R. J., Matus, A. V., Soden, B. J., & L'Ecuyer, T. S. (2019). Observation-based radiative kernels from CloudSat/CALIPSO. *Journal of Geophysical Research: Atmospheres*, 124, 5431–5444. <https://doi.org/10.1029/2018JD029021>
- Loeb, N. G., Doelling, D. R., Wang, H., Su, W., Nguyen, C., Corbett, J. G., et al. (2018). Clouds and the Earth's Radiant Energy System (CERES) Energy Balanced and Filled (EBAF) top-of-atmosphere (TOA) Edition-4.0 data product. *Journal of Climate*, 31(2), 895–918. <https://doi.org/10.1175/JCLI-D-17-0208.1>
- Loeb, N. G., Wang, H., Allan, R. P., Andrews, T., Armour, K., Cole, J. N. S., et al. (2020). New generation of climate models track recent unprecedented changes in Earth's radiation budget observed by CERES. *Geophysical Research Letters*, 47, e2019GL086705. <https://doi.org/10.1029/2019GL086705>
- Madden, R. A., & Julian, P. R. (1994). Observations of the 40-50-day tropical oscillation—A review. *Monthly Weather Review*, 122(5), 814–837. [https://doi.org/10.1175/1520-0493\(1994\)122<0814:OOTDTP>2.0.CO;2](https://doi.org/10.1175/1520-0493(1994)122<0814:OOTDTP>2.0.CO;2)
- Mauritsen, T., & Stevens, B. (2015). Missing iris effect as a possible cause of muted hydrological change and high climate sensitivity in models. *Nature Geoscience*, 8, 346–351. <https://doi.org/10.1038/ngeo2414>
- Muller, C., & Bony, S. (2015). What favors convective aggregation and why? *Geophysical Research Letters*, 42, 5626–5634. <https://doi.org/10.1002/2015GL064260>
- Muller, C. J., & Held, I. M. (2012). Detailed investigation of the self-aggregation of convection in cloud-resolving simulations. *Journal of the Atmospheric Sciences*, 69, 2551–2565. <https://doi.org/10.1175/JAS-D-11-0257.1>
- Orlanski, I. (1975). A rational subdivision of scales for atmospheric processes. *Bulletin of the American Meteorological Society*, 56(5), 527–530.

- Pendergrass, A. G., Reed, K. A., & Medeiros, B. (2016). The link between extreme precipitation and convective organization in a warming climate: Global radiative-convective equilibrium simulations. *Geophysical Research Letters*, 43, 11,445–11,452. <https://doi.org/10.1002/2016GL071285>
- Pierrehumbert, R. T. (1995). Thermostats, radiator fins, and the local runaway greenhouse. *Journal of the Atmospheric Sciences*, 52, 1784–1806. [https://doi.org/10.1175/1520-0469\(1995\)052<1784:TRFATL>2.0.CO;2](https://doi.org/10.1175/1520-0469(1995)052<1784:TRFATL>2.0.CO;2)
- Proistosescu, C., Donohoe, A., Armour, K. C., Roe, G. H., Stuecker, M. F., & Bitz, C. M. (2018). Radiative feedbacks from stochastic variability in surface temperature and radiative imbalance. *Geophysical Research Letters*, 45, 5082–5094. <https://doi.org/10.1029/2018GL077678>
- Qu, X., Hall, A., Klein, S., & Caldwell, P. (2015). The strength of the tropical inversion and its response to climate change in 18 CMIP5 models. *Climate Dynamics*, 45(1/2), 375–396.
- Radel, G., Mauritsen, T., Stevens, B., Dommenges, D., Matei, D., Bellomo, K., & Clement, A. C. (2016). Amplification of El-Niño by cloud longwave coupling to atmospheric circulation. *Nature Geoscience*, 9(2), 106–110. <https://doi.org/10.1038/ngeo2630>
- Rasmusson, E. M., & Carpenter, T. H. (1982). Variations in tropical sea surface temperature and surface wind fields associated with the Southern Oscillation/El Niño. *Monthly Weather Review*, 110(5), 354–384. [https://doi.org/10.1175/1520-0493\(1982\)110<0354:VITSST>2.0.CO;2](https://doi.org/10.1175/1520-0493(1982)110<0354:VITSST>2.0.CO;2)
- Semie, A. G., & Bony, S. (2020). Relationship between precipitation extremes and convective organization inferred from satellite observations. *Geophysical Research Letters*, 47, e2019GL086927. <https://doi.org/10.1029/2019GL086927>
- Soden, B. J., & Held, I. M. (2006). An assessment of climate feedbacks in coupled ocean-atmosphere models. *Journal of Climate*, 19(14), 3354–3360. <https://doi.org/10.1175/JCLI3799.1>
- Soden, B. J., Held, I. M., Colman, R., Shell, K. M., Kiehl, J. T., & Shields, C. A. (2008). Quantifying climate feedbacks using radiative kernels. *Journal of Climate*, 21(14), 3504–3520. <https://doi.org/10.1175/2007JCLI2110.1>
- Stein, T. H. M., Holloway, C. E., Tobin, I., & Bony, S. (2017). Observed relationships between cloud vertical structure and convective aggregation over tropical ocean. *Journal of Climate*, 30(6), 2187–2207. <https://doi.org/10.1175/JCLI-D-16-0125.1>
- Tobin, I., Bony, S., Holloway, C. E., Grandpeix, J.-Y., Sèze, G. A., Coppin, D., et al. (2013). Does convective aggregation need to be represented in cumulus parameterizations? *Journal of Advances in Modeling Earth Systems*, 5, 692–703. <https://doi.org/10.1002/jame.20047>
- Tobin, I., Bony, S., & Roca, R. (2012). Observational evidence for relationships between the degree of aggregation of deep convection, water vapor, surface fluxes, and radiation. *Journal of Climate*, 25, 6885–6904. <https://doi.org/10.1175/JCLI-D-11-00258.1>
- Tompkins, A. M. (2001). Organization of tropical convection in low vertical wind shears: The role of water vapor. *Journal of the Atmospheric Sciences*, 58(6), 529–545. [https://doi.org/10.1175/1520-0469\(2001\)058<0529:OOTCIL>2.0.CO;2](https://doi.org/10.1175/1520-0469(2001)058<0529:OOTCIL>2.0.CO;2)
- Tompkins, A. M., & Semie, A. G. (2017). Organization of tropical convection in low vertical wind shears: Role of updraft entrainment. *Journal of Advances in Modeling Earth Systems*, 9, 1046–1068. <https://doi.org/10.1002/2016MS000802>
- Weger, R. C., Lee, J., Zhu, T., & Welch, R. M. (1992). Clustering, randomness and regularity in cloud fields: 1. Theoretical considerations. *Journal of Geophysical Research*, 97(D18), 20,519–20,536. <https://doi.org/10.1029/92JD02038>
- Wing, A. A., & Cronin, T. W. (2016). Self-aggregation of convection in long channel geometry. *Quarterly Journal of the Royal Meteorological Society*, 142(694), 1–15. <https://doi.org/10.1002/qj.2628>
- Wing, A. A., & Emanuel, K. A. (2014). Physical mechanisms controlling self-aggregation of convection in idealized numerical modeling simulations. *Journal of Advances in Modeling Earth Systems*, 6, 59–74. <https://doi.org/10.1002/2013MS000269>
- Wing, A. A., Emanuel, K., Holloway, C. E., & Muller, C. (2017). Convective self-aggregation in numerical simulations: A review. *Surveys in Geophysics*, 38(6), 1173–1197. <https://doi.org/10.1007/s10712-017-9408-4>
- Wood, R., & Bretherton, C. S. (2006). On the relationship between stratiform low cloud cover and lower-tropospheric stability. *Journal of Climate*, 19(24), 6425–6432. <https://doi.org/10.1175/JCLI3988.1>
- Zhang, Y., & Fueglistaler, S. (2019). Mechanism for increasing tropical rainfall unevenness with global warming. *Geophysical Research Letters*, 46, 14,836–14,843. <https://doi.org/10.1029/2019GL086058>
- Zhou, C., Zelinka, M. D., & Klein, S. A. (2016). Impact of decadal cloud variations on the Earth's energy budget. *Nature Geoscience*, 9, 871–874. <https://doi.org/10.1038/ngeo2828>

# Observed modulation of the tropical radiation budget by deep convective organization and lower-tropospheric stability

S. Bony<sup>1</sup>, A. Semie<sup>1,2</sup>, R. J. Kramer<sup>3,4</sup>, B. Soden<sup>5</sup>, A. M. Tompkins<sup>6</sup>,  
and K. A. Emanuel<sup>7</sup>

<sup>1</sup>LMD/IPSL, Sorbonne University, CNRS, Paris, France

<sup>2</sup>Computational Data Science Program, Addis Ababa University, Addis Ababa, Ethiopia

<sup>3</sup>Climate and Radiation Laboratory, NASA Goddard Space Flight Center, Greenbelt, MD USA

<sup>4</sup>Universities Space Research Association, Columbia, MD USA

<sup>5</sup>RSMAS, University of Miami, Miami, FL, USA

<sup>6</sup>ICTP, Trieste, Italy

<sup>7</sup>MIT, Cambridge, MA, USA

## Contents of this file

1. Tables S1 to S3
2. Figures S1 to S10

---

Corresponding author: S. Bony, LMD/IPSL, Sorbonne University, CNRS, 4 Place Jussieu,  
Mail box 99, 75252 Paris cedex 05, France. ([sandrine.bony@lmd.jussieu.fr](mailto:sandrine.bony@lmd.jussieu.fr))

May 27, 2020, 12:11am

**Introduction** In this Supporting Information, we provide a table comparing the relationships obtained between the convective organization index and the radiation budget components for two different methods of computation of the organization index (Table S1), a table comparing the linear correlation coefficients of  $I_{org}$  and EIS with low-level, mid-level and high-level cloud amount derived from satellite observations (Table S2), a table comparing the linear correlation coefficients between  $I_{org}$  or EIS and the different components of the radiation budget computed by considering all months, by considering just ENSO events, or by excluding ENSO events (Table S3). We also provide an illustration of the detection of convective centroids using the 'local minimum method' (Fig. S1), examples of instantaneous satellite images and their convective organization index (Fig. S2), a plot showing time series of 3-hourly, daily, monthly and low-pass filtered  $I_{org}$  data (Fig. S3), a plot showing the relationship between the deep convective area and the convective organization index (Fig. S4), a figure similar to Fig. 7a but using an alternative method to compute the organization index (Fig. S5), a plot showing the co-variation of monthly anomalies of  $N$  with  $I_{org}$  and the tropical-mean fractional deep-convective area (Fig. S6), time series of daily and monthly data of  $I_{org}$ , EIS and  $N$  and the correlation between them (Fig. S7), maps of the sea surface temperature anomalies regressed onto convective organization anomalies or lower-tropospheric stability anomalies (Fig. S8), PDFs of the large-scale pressure vertical velocity in the mid-troposphere associated for low and high  $I_{org}$  regimes (Fig. S9), and power spectra of  $I_{org}$ , EIS,  $N$  and two indices characterizing tropical climate variability at intraseasonal and interannual timescale (Fig. S10).



**Table S1.** Linear correlation coefficients of the different components of the net radiation budget with the deep convective organization index  $I_{org}$  computed either with the local minimum method (as reported in Table 1) or with a clustering algorithm (the difference between the two methods is discussed in the section *Material and Methods*).

$I_{org}$	N	$N_{cs}$	CRE	$N_{lw}$	$N_{sw}$	$N_{cs,lw}$	$N_{cs,sw}$	$CRE_{lw}$	$CRE_{sw}$	MTH	EIS	SST	SOI
local min.	-0.65	-0.54	-0.43	-0.53	-0.22	-0.47	-0.33	-0.39	-0.13	-0.63	0.37	-0.05	-0.27
clustering	-0.66	-0.52	-0.48	-0.42	-0.35	-0.39	-0.43	-0.29	-0.23	-0.51	0.37	-0.14	-0.12

**Table S2.** Linear correlation coefficients of  $I_{org}$  and EIS with the low-level (surface to 680 hPa level), mid-level (between 440 and 680 hPa) and high-level (pressures lower than 440 hPa) cloud amount derived from the GOCCP CALIPSO lidar observations over the 2007-2017 period. Coefficients in brackets are not statistically significant.

	low-level clouds	mid-level clouds	high-level clouds
$I_{org}$	0.33	(-0.01)	-0.41
EIS	0.71	(-0.10)	(0.06)

**Table S3.** Linear correlation coefficients of the different components of the net radiation budget ( $N$ , with  $N = N_{cs} + CRE$ , where  $N_{cs} = N_{cs,lw} + N_{cs,sw}$ ;  $N_{cs,lw} = -OLR_{cs}$  and  $CRE = CRE_{lw} + CRE_{sw}$ ,  $CS$  referring to as "clear-sky" and  $CRE$  "cloud-radiative effect") with the deep convective organization index  $I_{org}$  and the lower-tropospheric stability  $EIS$  computed by considering all months of the 2001-2017 period, by excluding the months of this period that correspond to El-Niño or La-Niña conditions (defined as months for which the monthly anomaly of the tropical-mean SST exceeds 1.5 times the standard deviation of monthly SST values computed over the 1990-2017 period), or by restraining the sample to El-Niño and La-Niña conditions. Over a total of 204 months, 28 months correspond to El-Niño or La-Niña conditions.

	$N$	$N_{cs}$	$CRE$	$N_{lw}$	$N_{sw}$	$N_{cs,lw}$	$N_{cs,sw}$	$CRE_{lw}$	$CRE_{sw}$	$SST$
$I_{org}$ (all months)	-0.65	-0.54	-0.43	-0.53	-0.22	-0.47	-0.33	-0.39	-0.13	-0.05
$I_{org}$ (non ENSO)	-0.62	-0.56	-0.42	-0.52	-0.22	-0.50	-0.28	-0.35	-0.13	-0.04
$I_{org}$ (ENSO)	-0.71	-0.53	-0.42	-0.58	-0.14	-0.46	-0.53	-0.59	-0.03	-0.05
$EIS$ (all months)	-0.66	-0.44	-0.55	-0.36	-0.41	-0.47	-0.10	-0.09	-0.41	0.17
$EIS$ (non ENSO)	-0.68	-0.47	-0.57	-0.38	-0.42	-0.51	-0.08	-0.10	-0.42	0.19
$EIS$ (ENSO)	-0.57	-0.36	-0.41	-0.27	-0.35	-0.38	-0.11	0.01	-0.33	0.20

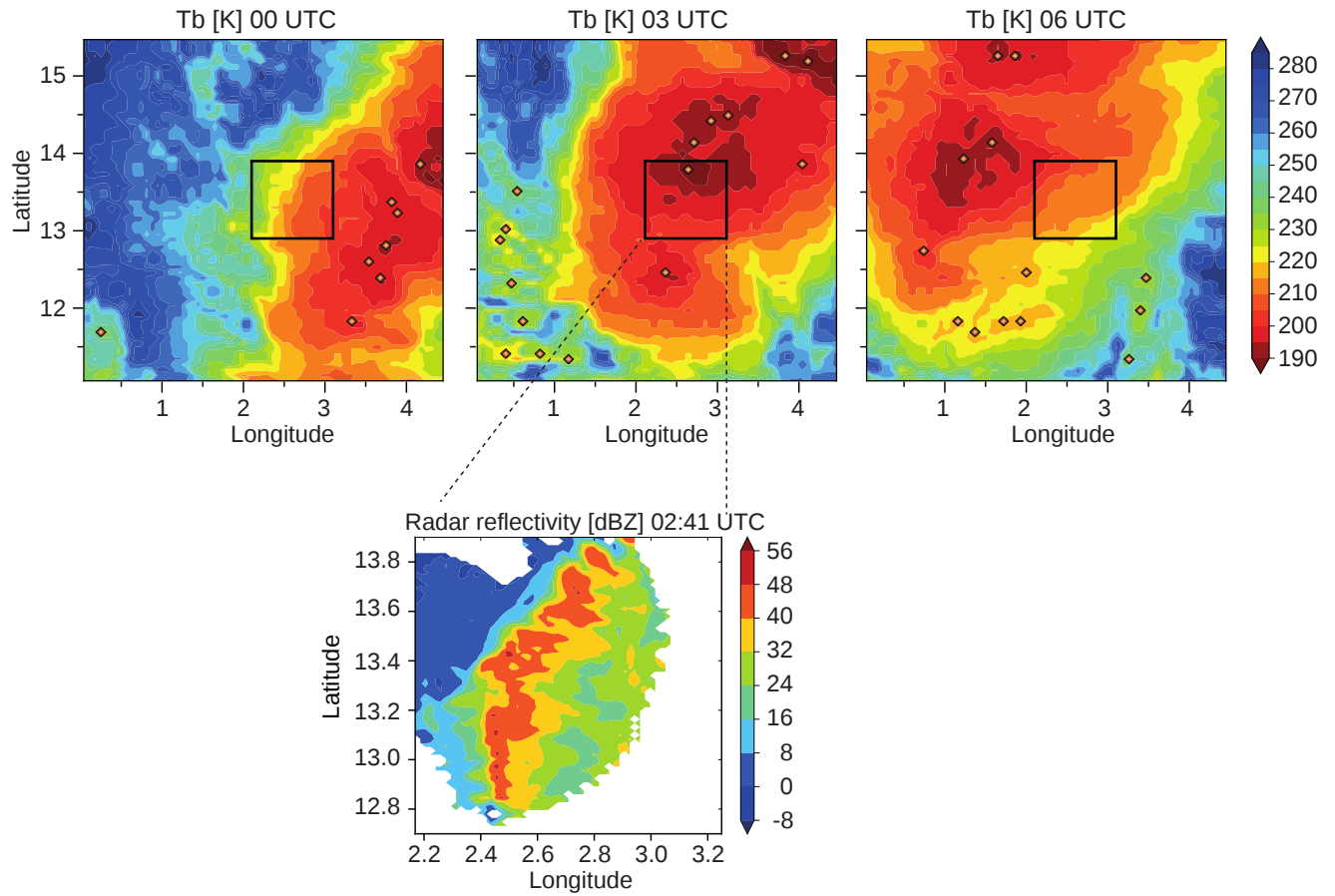


**Figure S1.** (Top) Series of 3-hourly snapshots of GridSat infrared brightness temperature data (in K) over the Sahel (around Niger) on 11 August 2006 overlaid by the deep convective centroids identified through the ‘local minimum method’ and (Bottom) radar reflectivity field (in dBZ) measured (on a smaller area) between 2:11 and 3:18 AM on August 11 2006 by the MIT C-band Doppler radar that was installed in Niamey during the AMMA field campaign. The rectangles overlaid on the upper-panel plots show the approximate area covered by the MIT radar. The squall line of Aug 11th 2006 is well captured by the deep convective centroids.

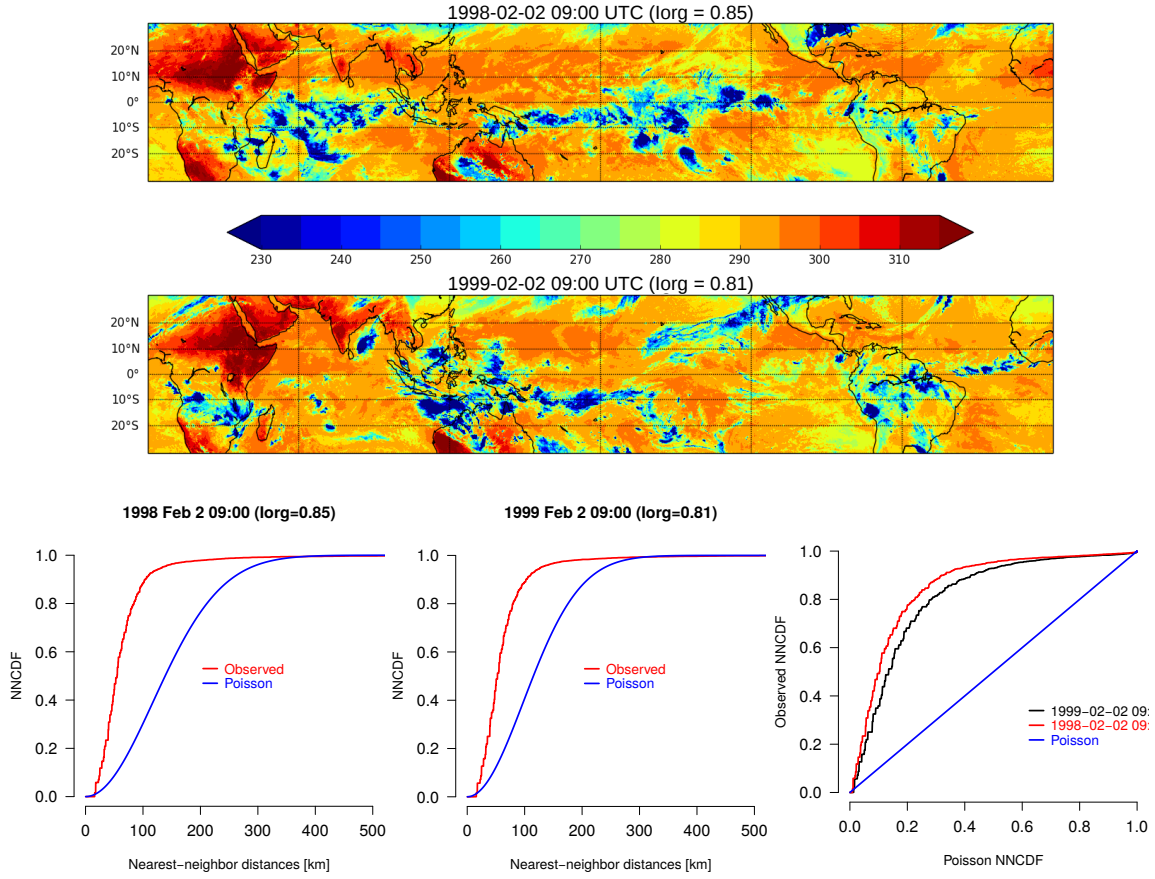


**Figure S2.** (Top) Snapshots of GridSat infrared brightness temperature data over the tropical belt on February 2 1998 and 1999 at 9 UTC. (Bottom) Calculation of the  $I_{org}$  index: panels show normalized cumulative distribution functions of the nearest neighbor distances (NNPDF) associated with the deep convective distribution of 09ZFeb02 in 1998 and in 1999. On the first two panels, the blue curve represents the NNPDF that would be predicted for a random distribution, while the colored curve represents the NNPDF of the actually observed distribution. The third panel shows the NNPDF derived from observations against the NNPDF associated with a Poisson distribution. The  $I_{org}$  index is calculated by integrating the area under the observed NNPDF (0.85 and 0.81 in the 1998 and 1999 cases, respectively).

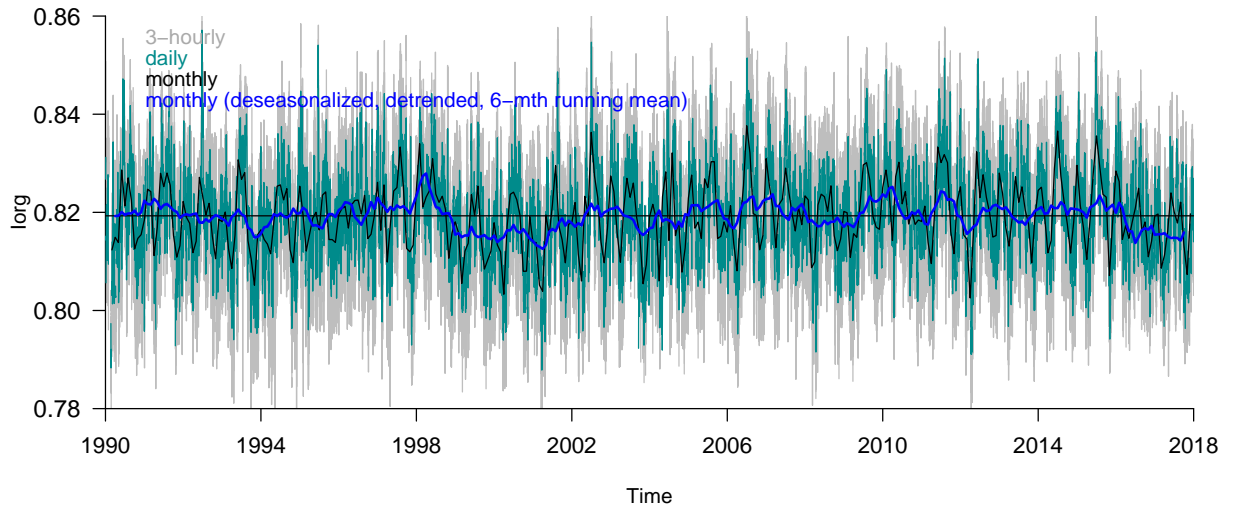


**Figure S3.** Time series of the convective organization index ( $I_{org}$ ) computed at the 3-hourly timescale (grey line), and once averaged at the daily (green line) and monthly timescales (black line). Also reported (thick blue line) is the time series (6-month running mean) of monthly deseasonalized and detrended  $I_{org}$  anomalies.



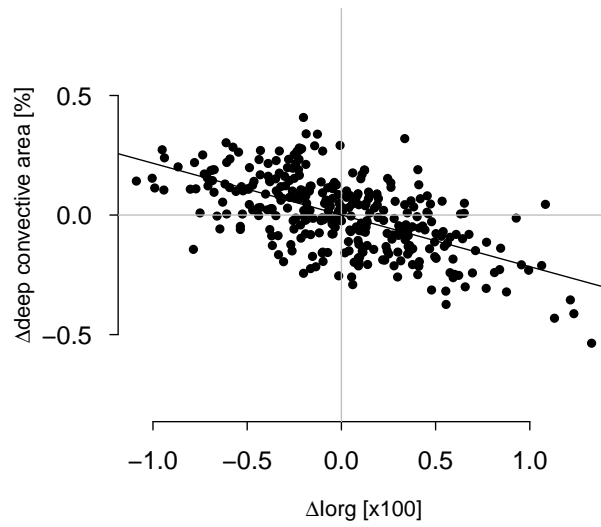


**Figure S4.** Scatter plot between anomalies of the deep convective area of the tropics (calculated as the area where  $T_b$  is lower than 240 K) and the convective organization index  $I_{org}$ . Also reported is the linear regression line across all points. Note that the tropically-averaged absolute value of the area covered by deep convection is 5.3%.

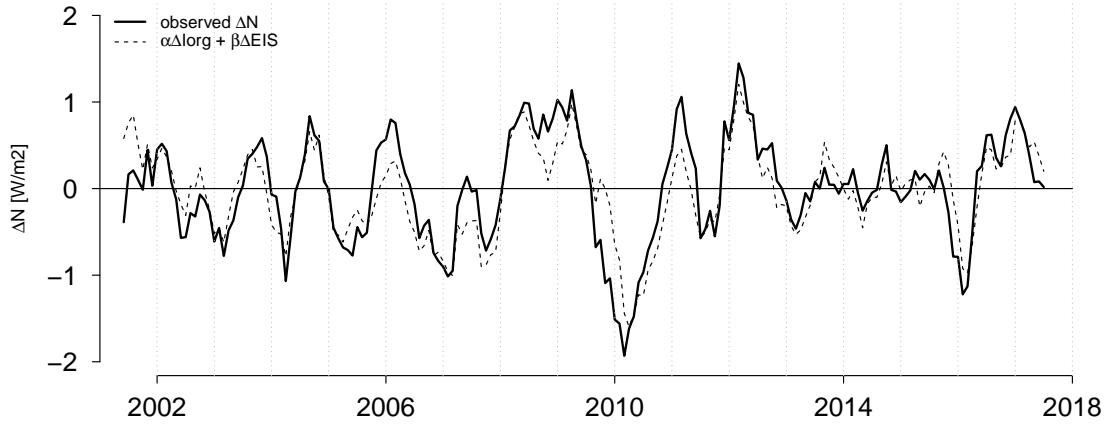


**Figure S5.** Time series of monthly anomalies of the tropically-averaged Earth radiation budget derived from CERES satellite observations (solid line) and reconstituted (dashed line) from  $\Delta I_{org}$  and  $\Delta EIS$  through linear multiple regression ( $\Delta N = \alpha \Delta I_{org} + \beta \Delta EIS$  with  $\alpha = -104.74 \text{ Wm}^2$  and  $\beta = -3.09 \text{ Wm}^2\text{K}^{-1}$ ), with  $I_{org}$  computed using the clustering method. The reconstruction of  $\Delta N$  using this method is as good ( $R^2 = 0.64$ ) as when using the local minimum method ( $R^2 = 0.62$ , Figure 7). A 6-month running mean has been applied for the plotting; for these low-pass filtered data,  $R^2 = 0.71$ .

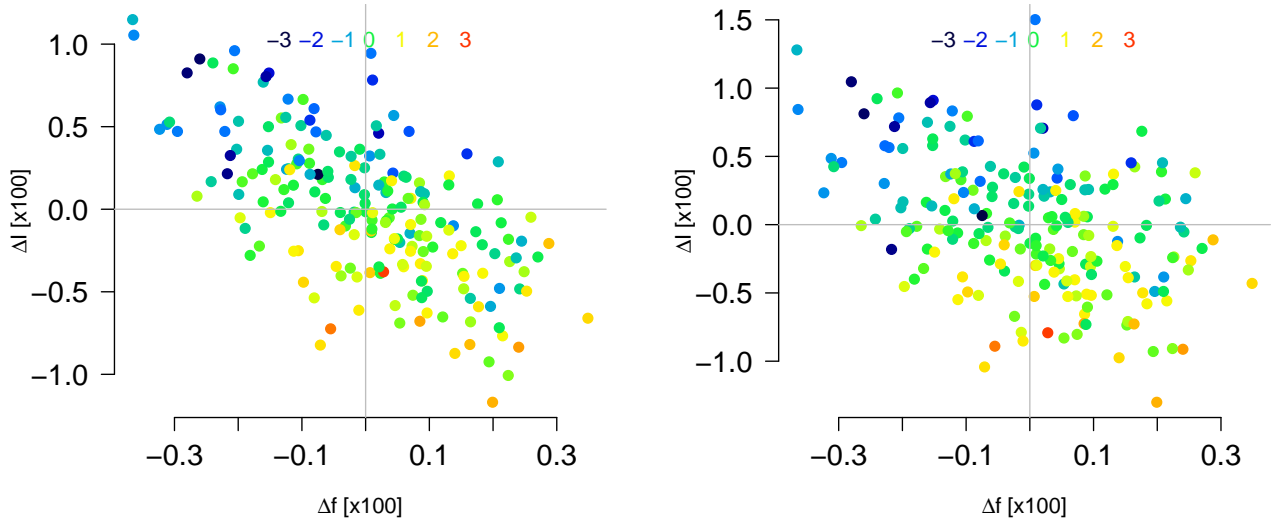


**Figure S6.** Relationship between monthly (deseasonalized and detrended) anomalies of the net radiation budget ( $\Delta N$ ,  $\text{Wm}^{-2}$ , in color) and anomalies of the convective organization index ( $\Delta I_{org}$ , computed either through the local minimum approach, left, or through the clustering approach, right) and the tropical deep-convective area fraction ( $\Delta f$ ,  $f$  defined by the area of the tropics covered by  $T_b < 240$  K). The anti-correlation between  $\Delta N$  and  $\Delta I_{org}$  holding for a given  $\Delta f$ , it is not primarily explained by the relationship between  $N$  and  $f$ . Consistently, the partial correlation between  $\Delta N$  and  $\Delta I_{org}$  for a given  $f$  equals -0.58 ( $I_{org}$  computed through the local minimum approach) or -0.60 (clustering approach), i.e. hardly less than the full correlation between  $\Delta N$  and  $\Delta I_{org}$  (-0.65 and -0.66, for the local minimum and the clustering approaches, respectively).

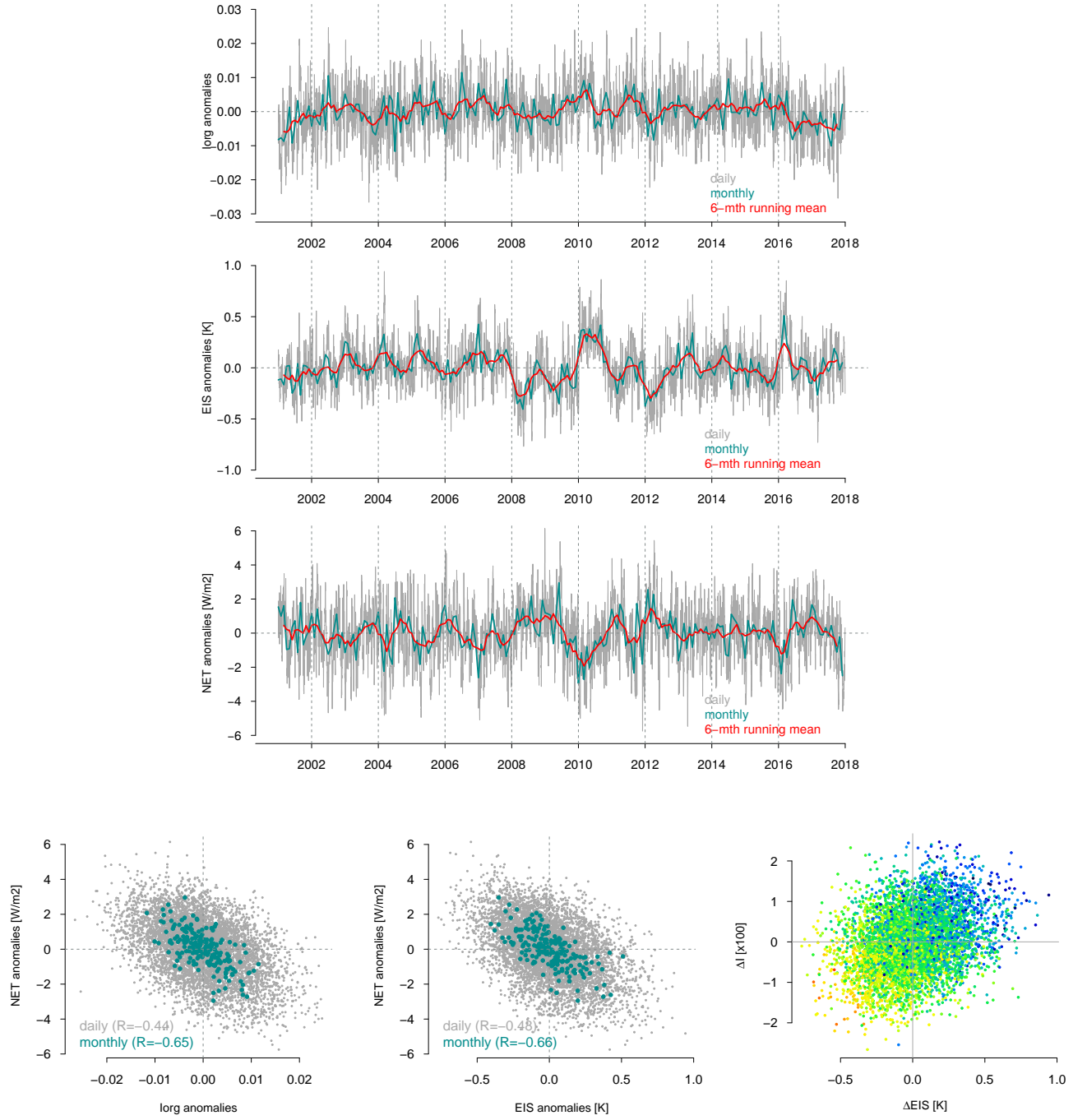


**Figure S7.** Time evolution of daily and monthly variations of (top) the convective organization index ( $I_{org}$ ) and (middle) of the net radiation budget ( $N$ ). All anomalies are deseasonalized and detrended. Also reported is the 6-month running mean of the monthly deseasonalized and detrended variations. (bottom) Relationship between  $I_{org}$  and  $N$  anomalies at the daily (grey markers) and monthly (green markers) timescales.

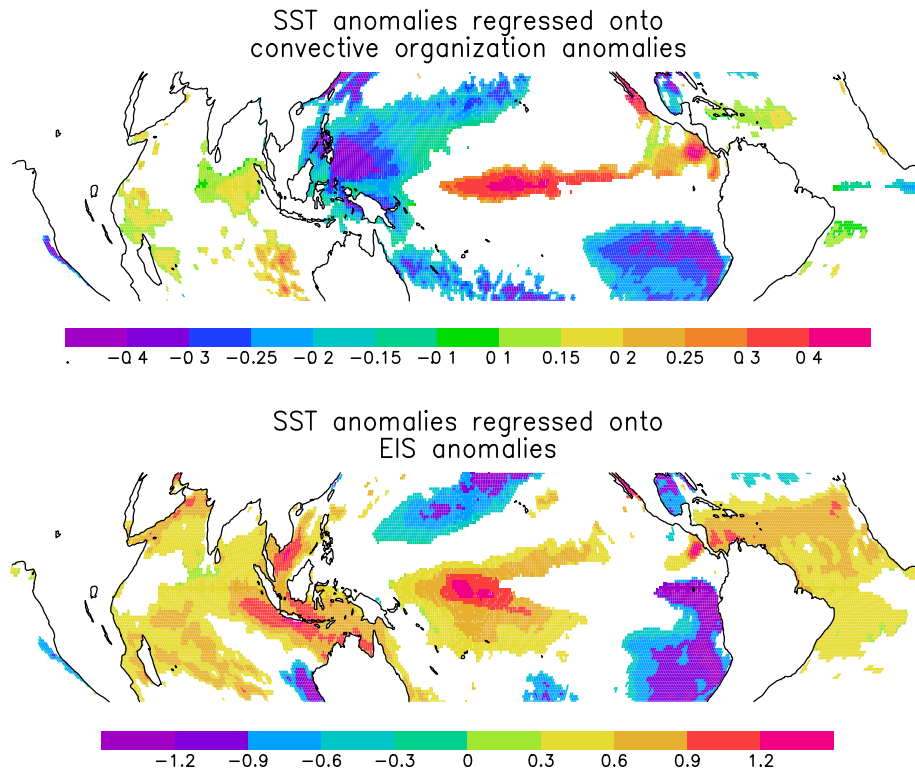


**Figure S8.** Spatial distribution of sea surface temperature anomalies regressed onto (a)  $I_{org}$  or (b)  $EIS$  monthly anomalies over 2001-2017.  $I_{org}$  and  $EIS$  are associated with different SST patterns, especially over the Indian and Atlantic oceans. Results are reported only in regions where the linear regression is statistically significant (p-value < 0.05). Units: K/( $I_{org}$ ) and K/K, respectively.



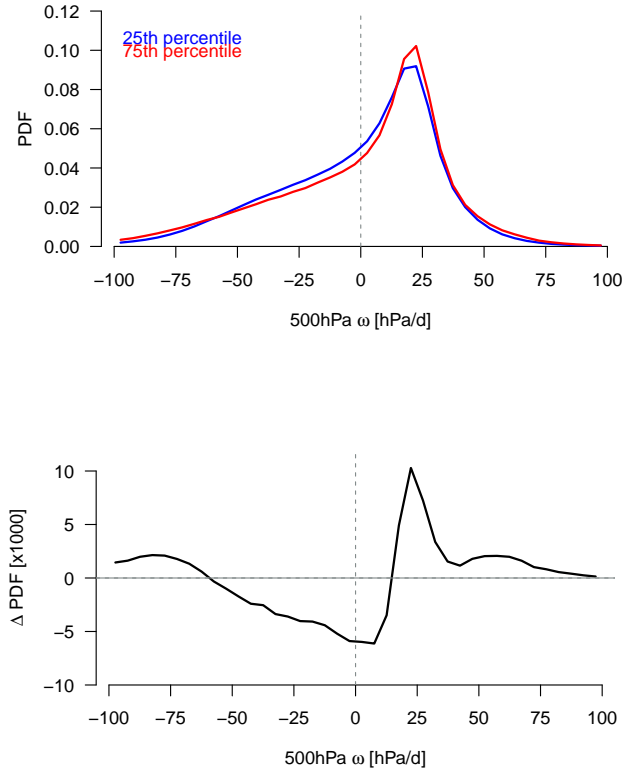


**Figure S9.** (top) Mean probability distribution function (PDF) of large-scale vertical velocity at 500 hPa within 30°S-30°N (derived from monthly ERA interim reanalyses) associated with the first and last quartiles of the  $I_{org}$  distribution during 1990-2017. (bottom) Difference between the two PDFs (75<sup>th</sup> percentile minus 25<sup>th</sup> percentile of  $I_{org}$ ). Higher values of the convective organization index are associated with a strengthening of the large-scale overturning circulation.

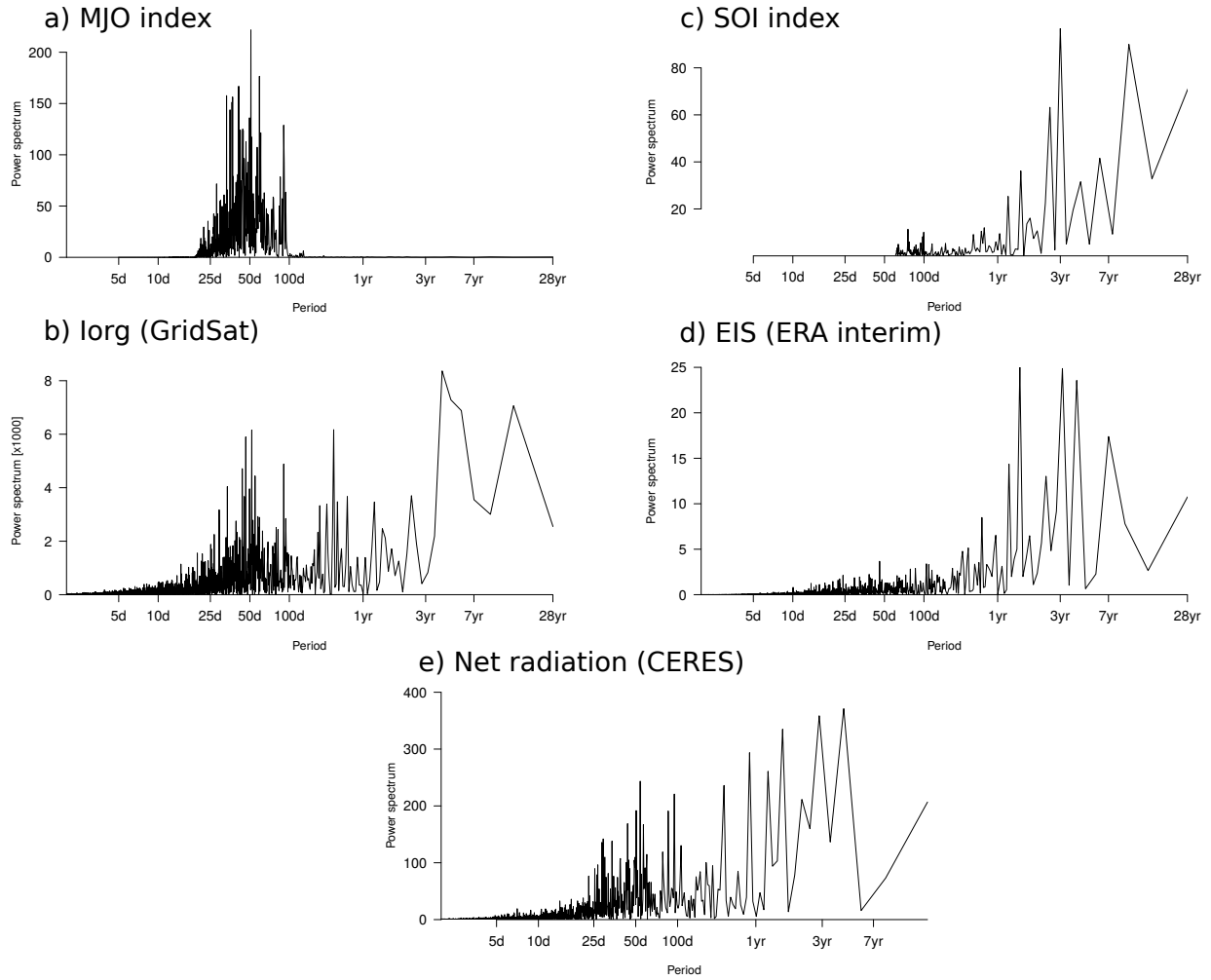


**Figure S10.** Power spectrum of (a) the daily Madden-Julian Oscillation index (OMI PC1 index) from Kiladis G.N. et al., A comparison of OLR and circulation based indices for tracking the MJO. *Monthly Weather Review*, 142 1697-1715, 2014) (b) the daily  $I_{org}$  index (deseasonalized and detrended anomalies) of deep convective organization from GridSat data, (c) the monthly Southern Oscillation Index (SOI) from NOAA, (d) the daily lower-tropospheric stability EIS (deseasonalized and detrended anomalies) from ERA interim reanalyses and (e) the daily tropically-averaged net radiation budget from CERES data (deseasonalized and detrended). All spectra are computed over the period 1990-2017, except CERES data which are available for 2001-2017 only.